Kinetic and Magnetic Large Scale Forcing in Magnetohydrodynamics

Adam Chalupa

August 19, 2016

MSc in Theoretical Physics

The University of Edinburgh

2016

Abstract

Magnetohydrodynamics (MHD) describes the turbulent dynamics found within conductive fluid flows. Due to the non-linear nature of turbulence, it has been speculated that the behaviour of systems at large Reynolds numbers should not depend on the manner in which they were originally agitated, i.e. similar results should be produced. If a system initially begins turbulent but lacks further means of agitation, it will quickly decay away through the energy cascade. Therefore, a forcing term must be added to the MHD equations to ensure an energetically steady state. We simulate and investigate three-dimensional MHD turbulent systems through using three statistically isotropic and homogeneous methods of forcing energy in MHD non-compressible fluids. We find a partial agreement in our energy spectra with the theoretical large Reynolds number limit IK spectra, and confirm similar behaviours between the kinetic introduction of the three different forcing methods. We also investigate what occurs when the magnetic field is forced through two of the three methods, producing dissimilar results to one another.

Declaration

I declare that all work composed and written into this document, unless stated otherwise, is my original work and authorship. The technology and simulation software utilized to derive the results presented here are the work of Dr. Sam Yoffe and Dr. Moritz Linkmann.

In the duration of this project I was consulted by Dr. Arjun Berera, Mairi McKay, and Dr. Moritz Linkmann for help on the interpretation of my results. All results presented were configured, recorded, and run by myself. The simulations were conducted on Archer (http://www.archer.ac.uk/) and the University of Edinburgh's Eddie cluster with the permission and allocation of resources from the turbulence group at the University of Edinburgh.

In this report, certain results are considered and build upon from a prior similar project conducted by Daniel Clark (MPhys) along with the turbulence group at the University of Edinburgh, and with permission is credited when any result of theirs is referenced.

The visualizations presented in the final section of our results were made through the open source program Paraview (http://www.paraview.org/).

Adam A. Chalupa, August 2016

Contents

1 Introduction **1**

2 Hydrodynamical Theory and MHD **3**

2.1 Equations of Fluid Motion 3

2.1.1 Reynolds Number 5

2.1.2 Navier Stokes Fourier Transforms 5

2.1.3 The Vorticity Equation 7

2.2 Kolmogorov Scales and the Energy Cascade 8

2.2.1 Kolmogorov's Hypothesis 8

2.2.2 The Energy Cascade and Transfer Functions 10

2.3 Extension to Magnetohydrodynamics 12

2.3.1 MHD Equations 12

2.3.2 Derivation of the MHD Equations 13

2.3.3 The Induction Equation 14

2.3.4 Ideal Conserved Quantities in MHD 16

2.3.5 Universality and Forcing the MHD Equations 21

2.3.6 Fourier Transform of the MHD Equations 22

2.4 Self-Organization in MHD 24

2.4.1 Beltrami and Alfvénic Fields 24

2.4.2 The Inverse Cascade 25

2.4.3 The Dynamo Effect 26

3 Method and Direct Numerical Simuations **27**

3.1 Pseudospectral DNS 27

3.2 Computing Techniques 29

3.2.1 Initial Fields and Anti-aliasing 29

3.2.2 Checking and Running the Code 29

3.3 Forcing Functions for Isotropic Turbulence 30
3.3.1 Negative Damping 31
3.3.2 Adjustable Helicity 32
3.3.3 Sinforce 33

4 Results **35**
4.1 Kinetic Forcing 35
4.1.1 Energy Over Time 36
4.1.2 Helicities 38
4.1.3 Energy and Cross Helicity Correlation 39
4.1.4 Energy and Transfer Spectra 42
4.1.5 Kinetic Forcing Summary 44
4.2 Magnetic and Kinetic Forcing 44
4.2.1 Negative Damping Forcing 45
4.2.2 Adjustable Helicity Forcing 48
4.2.3 Magnetic Forcing Summary 52

5 Conclusions **54**

A Run Input Parameters **56**
A.1 Input Parameters 56

List of Tables

A.1 A list of basic run parameters used for kinetically forcing MHD systems. Systems with run times $< 100s$ were not included in our results. 56

A.2 A list of basic run parameters used for magnetic/kinetic forcing in MHD systems. Systems with run times $< 100s$ were not included in our results. 57

List of Figures

4.1 Three figures of magnetic and kinetic energy vs. time marked with their respective forcing method and at system size 128^3. All Re values are taken as an average from $t = 20s$ to $t = 100s$. Note that the SF diagram has a slightly higher Re due to the slight contribution from the large spike of kinetic energy around $t \sim 10s$. 36

4.2 Three figures of magnetic and kinetic energy vs. time marked with their respective forcing method at system size 256^3. All Re values are taken as an average from $t = 20s$ to $t = 100s$. We see the same SF behaviour, where a large spike of energy occurs in the beginning and dies down at $t = 20s$. 37

4.3 Relative cross and magnetic helicities using AHF at system size 256^3 and $Re = 399.3$ (a). Note that in (a), there appears to be a buildup in cross helicity. However, in (b) we used the same forcing method at a similar $Re = 334.9$, leading us to believe this buildup in (a) is more likely a fluctuation. 38

4.4 Relative helicities for varying system sizes/forcing types and low to high Reynolds numbers. Note that for SF in (e), (f), as we increase Re the fluctuations in the relative magnetic helicity decrease, but for cross helicity they remain relatively the same. 39

4.5 Energy vs. time plots (presented previously for 256^3 systems) with slices placed to indicate interesting energetic behaviours, e.g. where the kinetic energy drops and magnetic energy appears to rise. We seek to find a correlation between the relative helicities (right column) at these points in energy. 40

4.6 The magnetic energy spectra with each forcing method and similar Re plotted with each other. Diagram (a) shows systems of $Re \sim 105$ and (b) shows systems of $Re \sim 345$. Each diagram is plotted with the IK power law. 42

4.7 The ensemble average kinetic and magnetic transfer spectra for 128^3 and 256^3 and kinetic negative damping, adjustable helicity, and sinusoidal forcing. Negative values indicate energy flowing out of those wavenumbers, positive indicating energy is flowing in. 43

4.8 Energy for a 128^3 system forced with ND run for 270 seconds. Notice after 25 seconds there occurs a self-organized state. 45

4.9 Relative cross and magnetic helicities using ND forcing both kinetically and magnetically. Notice that though the simulations were nearly similar in their input parameters, they produce opposite valued cross helicities. This is due to the randomized initial directions of the $\boldsymbol{U}$ and $\boldsymbol{B}$ fields, in (b) we see they align together whereas (a) in they anti-align. 46

4.10 Flow visualizations of 128^3 ND kinetic and magnetic forcing at different simulation times. The blue vectors indicate the magnetic field, the red indicate the velocity field. Notice that as our simulation time increases, the fields become more Alfvénic and anti-aligned with each other ($\boldsymbol{U} \sim -\boldsymbol{B}$). 47

4.11 Isosurfaces for the magntiude of the magnetic and velocity fields with ND magnetic/kinetic forcing at $t = 100s$. These depict large scale self-organized structures found in our flow. 48

4.12 Run Bb, energy and relative helicities derived from AHF magnetic/kinetic forcing done on a system of size 128^3. Notice the interesting increase in magnetic energy in correlation to the relative cross helicity at $t \sim 50s$. . . 49

4.13 Run Bb-s1, identical input parameters were used for this AHF magnetic/kinetically forced system of size 128^3, but a different seed value was introduced. The system exhibits a similar behaviour to what has been shown previously, but fails to emulate the actions of kinetic energy, magnetic energy, and relative CH. 50

4.14 Run Bb-s2, a third run of identical parameters with a different seed for AHF kinetic/magnetic forcing on system sizes of 128^3. We note that the behaviours seen in this system differ from both, given there are no large scale fluctuations in energy or relative helicity. 51

4.15 Flow visualizations for the magnetic fields from the first two presented runs, colors depict the magnitude of the field's vectors (red being the highest). Several partially self-organized structures can be seen, depicted by the spirals shown in the field lines. 52

Acknowledgements

Thank you to Dr. Arjun Berera and Mairi McKay, your insight and guidance in this project has been critical and helpful both for the direction and interpretation of the results. Mairi, thank you especially for all the time taken to meet with me and the punctual responses to all my long emails.

Thank you, Dr. Moritz Linkmann, for your insight and help with the interpretation of my magnetic forcing results and training in Paraview, it was invaluable.

Leta, thank you for your love, patience, support and for coming across the ocean with me. You have been a rock and foundation for me. Thank you Nick and Aaron, for your humour and support given to me while tackling your own difficult MSc projects.

Chapter 1

Introduction

Hydrodynamic systems, such as water moving through a pipe or pouring into a reservoir, often can be mathematically difficult to describe. This difficulty arises from the occurrence of turbulence, when the properties of the fluid can chaotically change in non-linear progression. We model and describe non-compressible Newtonian fluid systems through the usage of the Navier-Stokes equations. These are a set of coupled differential equations commonly used by theoretical dynamicists and fluid engineers alike, and can be computationally demanding to solve when one wants to simulate large turbulent flows.

The hydrodynamic (HD) Navier-Stokes equations, however, cannot fully describe a system of turbulent conducting fluid, such as plasma. This is made possible through the use of the Magnetohydrodynamic (MHD) equations. Similar in nature to the Navier-Stokes equations, the MHD equations encompass the usual fluid dynamics but through Maxwell's laws also consider the added effects of internal induced/external magnetic fields, like from the movement of turbulent charged particles in a fluid. MHD was first investigated by Michael Faraday in 1832. He believed that because of electrically conductive salt water flowing under Waterloo bridge and passing through the Earth's magnetic field, an induced current should be present and exert an electromotive force. Though he was initially unsuccessful in detecting this force due to the crudeness of his instruments, it was proven to be true years later in 1851 [1].

Viscous forces at small enough scales cause energetically diffusive effects, understood through the energy cascade that occurs from large to small scales in HD and partially in MHD. This diffusive effect is what causes turbulence to be a decaying process, that is, without the addition of energy into the system all kinetic energy will eventually pilfer out in the form of heat at very small scales. This brings about the need for a method of forcing which is uniformly invariant. It was hypothesized by Kolmogorov in 1941 that even with anisotropy at larger scales, as energy cascades down it loses this large scale information, and homogeneity /isotropy is found at the smaller scales [2]. As turbulence is non-linear, the technique used to agitate a system should produce independently identical turbulent end state behaviours. This brings about the purpose of this thesis report, to investigate the differences of an MHD isotropic/homogeneous turbulent fluid system, if any, through comparing different methods of forcing the system into such a state.

The advent of high powered parallel computing has garnered greater amounts of attention towards the simulation of turbulent fluid systems. Computing methods, such as Direct Numerical Simulations (DNS), allow for very accurate representations through very large to small scale simulations of dynamic and chaotic fluid systems. If one considers a very large, boundary-less system, it is possible to investigate turbulence which is statistically (since many independent points are considered in an ensemble average) homogeneous (translationally invariant) and isotropic (rotationally invariant). This is of importance because it greatly simplifies the dynamics of the turbulent fluid, and allows us to investigate the more fundamental behaviours of MHD (systems of finite boundaries would add complexities such as mean flows). An understanding of these fundamental behaviours are linked to the prospect of universality: much can be known about a turbulent MHD flow only from the knowledge of a few fundamental initial parameters. As stated before, due to the non-linear nature of how turbulence progresses in a fluid, it has been speculated that the manner in which a fluid is forced into a turbulent state should not affect the characteristics of the system after a large amount of time. We investigate this through the usage of three different methods (negative damping, adjustable helicity, and sinusoidal forcing) and through two different manners of forcing: kinetically and magnetically. The mathematics behind these different forcing methods are discussed in section 3.3.

To obtain our results, a software was used that solves the MHD equations of kinetic and magnetic motion. Given there can be no large scale mean fluctuations (we require our fields to be divergenceless, e.g. for fluid velocity $\boldsymbol{U}$, $\nabla \cdot \boldsymbol{U} = 0$) we solve for the field of interest's fluctuations. Simulation results were only viable once the MHD simulations were observed to be in an energetically 'steady state;' That is, when the energy dissipating out is equal to the amount being introduced in by an energetic forcing. The software used was a pseudospectral Direct Numerical Simulation (DNS) program written by S. Yoffe [3] and edited for MHD by M. Linkmann [4]. An understanding and potentially universal application of this end steady state behaviour could have beneficial effects on our predictions made from viewing MHD non-linear progressions in very large scale turbulent systems, such as coronal accretion disks or galaxy formations [5] [6] [7].

In the following two chapters of this report, we present necessary background required for the coherent understanding of presented results in section 4. Section 2 includes HD/MHD theory, derivation of the MHD equations, ideal conserved quantities and spectral representations of our equations of motion. In section 3, we introduce the fundamentals to our pseudospectral DNS and elucidate the forcing methods used in the simulation software. Negative damping was originally written into the software by S. Yoffe, who originally it for hydrodynamical simulations. The second method, adjustable helicity, was implemented by M. Linkmann while adapting the code for MHD. Finally, the third sinusoidal method was written into the MHD version by E. Goldstraw in her report [8]. A further investigation into homogeneously/istropically forced MHD was made by D. Clark [9], who lightly touched on the third method: sinusoidal forcing. We expand upon D. Clark's results through extending simulation times and addressing certain behaviours seen in the ideal conserved quantities (e.g. magnetic helicity). However, all previous result's systems only emphasized kinetic forcing (that is, forcing the equation of motion for velocity in the MHD equations). We investigate alongside of this kinetic forcing a magnetic method of forcing as well, which brings about interesting turbulent behaviours.

Chapter 2

Hydrodynamical Theory and MHD

This chapter introduces the reader to the essentials for understanding fluid dynamics and its extension into Magnetohydrodynamics (MHD). We begin by stating conservation laws for incompressible Newtonian fluids and deriving the Navier-Stokes equation. Then, we discuss a periodic systemic approach to turbulence, invoking the usage of Fourier analysis to solve for velocity through its equivalent Fourier series. This section also gives a background in different computational scales, important for understanding the extent of length scales a simulation should begin and end at. Furthermore, we transition into MHD theory, derive the MHD equations, and end with a brief section on how energetic isotropic /homogeneous forcing is imposed.

This chapter is structured in two parts: HD and MHD. This is so that the reader might obtain a grip on the fundamentals of fluid mechanics, and notice the eloquent extension of them into MHD. We do this to help identify how MHD theoretically follows very similar pathways with HD. If not specified otherwise, the Einstein summation rule will apply for all following equations. All field values, if not explicitly displayed, are functions of both space and time (e.g. for velocity $\boldsymbol{U} = \boldsymbol{U}(\boldsymbol{x},\ \mathrm{t}) = U_\alpha$). Any decimal numbers, unless specific otherwise, that appear in the text can be assumed as equation numbers ($2.95 = eqn.2.95$).

2.1 Equations of Fluid Motion

We begin by deriving the Navier Stokes equations, a set of coupled differential equations used to describe the flow of viscous fluids. To quantify the continuous nature of the fluid, we consider a sample size volume flow velocity: $\boldsymbol{U}(\mathbf{x},\mathrm{t})$. Note that $\boldsymbol{U}$ is a Eulerian field, given it is indexed by position $\mathbf{x}$ and is in an inertial frame. The mass and momentum conservation equations for an incompressible fluid (ρ = constant) are given respectively by:

$$\partial_\alpha U_\alpha = 0 \tag{2.1}$$

$$\partial_t U_\alpha + U_\beta \partial_\beta U_\alpha = -\frac{1}{\rho}\partial_\alpha p + \frac{1}{\rho}\partial_\beta s_{\alpha\beta} \tag{2.2}$$

Where p is the pressure of the fluid, ρ the density (we assume constant), and $s_{\alpha\beta}$ the deviatoric stress tensor. The values for α, β can be 1, 2, or 3. For a Newtonian fluid, $s_{\alpha\beta}$ is given by:

$$s_{\alpha\beta} = \rho\nu(\partial_\beta U_\alpha + \partial_\alpha U_\beta) \tag{2.3}$$

and ν is the kinematic viscosity (resistance against change) of the fluid. With the substitution of eqn. 2.3 into 2.2, we arrive at:

$$\partial_t U_\alpha + U_\beta \partial_\beta U_\alpha = -\frac{1}{\rho}\partial_\alpha p + \partial_\beta(\nu(\partial_\beta U_\alpha + \partial_\alpha U_\beta)) \tag{2.4}$$

Before continuing onward, for the sake of clarity, we derive the mass conservation (2.1) from the mass continuity equation:

$$\partial_t \rho + \partial_\alpha(\rho U_\alpha) = 0 \tag{2.5}$$

Then, as ρ is constant, $\partial_t \rho = 0$, giving us:

$$\nabla \cdot \boldsymbol{U} = 0 \tag{2.6}$$

We can use this conservation equation to cancel out the second term in eq 2.4, giving us the Navier Stokes equation:

$$\partial_t U_\alpha + U_\beta \partial_\beta U_\alpha = -\frac{1}{\rho}\partial_\alpha p + \nu \partial_{\beta\beta} U_\alpha \tag{2.7}$$

or

$$\partial_t \boldsymbol{U} + (\boldsymbol{U} \cdot \nabla)\boldsymbol{U} = -\frac{1}{\rho}\nabla p + \nu \nabla^2 \boldsymbol{U} \tag{2.8}$$

for hydrodynamic systems of constant density. This equation describes in entirety hydrodynamic flows and turbulence for incompressible Newtonian fluids. The non-linear term $(\boldsymbol{U} \cdot \nabla)\boldsymbol{U}$ in 2.8 presents an added difficulty for finding the solution, $\boldsymbol{U}$, and is responsible for kinetic energy transferring from large to small scales. With added detail, this mechanic is discussed in the following sections. The $\nu\nabla^2\boldsymbol{U}$ is the viscous dissipative term, and is dominant when flows are laminar (that is, non-turbulent) as it is proportional to velocity and viscosity. It should also be noted that in Fourier space, $\nabla^2 \to k^2$, so also at larger wavenumbers the dissipation is more dominant.

Homogeneous and Isotropic Turbulence

Isotropy and *homogeneity* are used to simplify the statistical examination of a forced turbulent fluid. Homogeneity ensures that our system's turbulence is translationally invariant, whereas isotropy ensures it is rotationally invariant. When flows become non-homogeneous or anisotropic, certain patterns such as sheers or mean flows can occur, which heavily alter the outcomes of our results. These properties are assumed when it comes to the probability distribution of the fluid's velocity, not the instantaneous values at any given time step. As there cannot be any mean flows (e.g. $\langle \boldsymbol{U} \rangle = 0$), then the velocity solved for in 2.8 must be fluctuations of the velocity [3].

We introduce a kinetic homogeneous/isotropic forcing term in the N-S equation (2.8) by:

$$\partial_t \boldsymbol{U} + (\boldsymbol{U} \cdot \nabla) \boldsymbol{U} = -\frac{1}{\rho} \nabla p + \nu \nabla^2 \boldsymbol{U} + \boldsymbol{F}_k \tag{2.9}$$

This kinetic forcing term, $\boldsymbol{F}_k$, is used to inject energy into the system at a set rate. Eventually, if a steady state is found, kinetic energy is homogeneously injected in at the same rate which is dissipating out through the dissipation term: $\nu \nabla^2 \boldsymbol{U}$. This is made evident by a constant mean value of total energy over time. When we introduce the MHD equations, the same technique will be used for forcing the MHD systems. For the scope of this report, we investigate only the homogeneous and istropic turbulence in MHD systems.

2.1.1 Reynolds Number

Characterizing the turbulence of a flow is done through the usage of a dimensionless parameter, the Reynolds Number. The Reynolds Number is the ratio between inertial (resistant to motion) and viscous (opposition to opposite flow) forces, and is defined by:

$$Re = \frac{\boldsymbol{U} l}{\nu} \tag{2.10}$$

Where $\boldsymbol{U}$ is the flow velocity, l the characteristic length scale, and ν the kinematic viscosity. The 'critical value' of a Reynolds number signifies a point where flow begins to transition from laminar (smooth) to turbulent. This is often within a range, for instance, flow through a pipe can remain laminar anywhere within: $Re < \sim 2000$ [10].

2.1.2 Navier Stokes Fourier Transforms

Converting the Navier-Stokes equation into Fourier space is commonly done when using pseudo-spectral calculation methods. Our system is defined to be homogenous and periodic, so we may express the velocity as a Fourier series and all differentiation (in $\boldsymbol{x}$ space) becomes multiplication. This technique also allows us to eliminate the pressure from the N-S equation through the usage of a non-local convolution. In later sections we use the theory found in this section to describe how our code uses Fast Fourier Transforms (FFT) to calculate turbulence and reduce calculation time. For example, derivatives are easier processed in $\boldsymbol{k}$ space, and non-linear terms in configuration space.

We begin by expressing the Fourier transform of the fluid velocity in $\boldsymbol{k}$ space as:

$$U_\alpha(\boldsymbol{k}, t) = \left(\frac{1}{2\pi}\right)^3 \int d\,^3x U_\alpha(\boldsymbol{x}, t) e^{-i\mathbf{k}\cdot\mathbf{x}} \tag{2.11}$$

And derive a continuity relation by taking the Fourier transform of eq. 2.1:

$$\mathcal{F}[\partial_\alpha U_\alpha(\boldsymbol{x},t)] = k_\alpha U_\alpha(\boldsymbol{k},t) = 0 \tag{2.12}$$

This continuity equation states the requirement that the velocity be orthogonal to its wavevector, $\boldsymbol{k}$.

Taking the Fourier transform of the entire hydrodynamic Navier-Stokes equation (2.8) gives us:

$$\partial_t \boldsymbol{U}(\boldsymbol{k},t) + \mathcal{F}[(\boldsymbol{U}(\boldsymbol{x},t)\cdot\nabla)\boldsymbol{U}(\boldsymbol{x},t)] = \frac{\boldsymbol{k}}{i\rho}p(\boldsymbol{k}) - \nu k^2 \boldsymbol{U}(\boldsymbol{k},t) \tag{2.13}$$

or

$$(\partial_t + \nu k^2)\boldsymbol{U}(\boldsymbol{k},t) + \mathcal{F}[(\boldsymbol{U}(\boldsymbol{x},t)\cdot\nabla)\boldsymbol{U}(\boldsymbol{x},t)] = \frac{\boldsymbol{k}}{i\rho}p(\boldsymbol{k},t) \tag{2.14}$$

where the second term is a non-linear velocity expression. To take its transform, we express it as a convolution. First, note that:

$$\mathcal{F}[(\boldsymbol{U}(\boldsymbol{x},t)\cdot\nabla)\boldsymbol{U}(\boldsymbol{x},t)] = \mathcal{F}\Big[U_\alpha(\boldsymbol{x},t)\frac{\partial U_\beta(\boldsymbol{x},t)}{\partial x_\alpha}\Big] \tag{2.15}$$

in this notation then:

$$\begin{aligned}\mathcal{F}\Big[U_\alpha(\boldsymbol{x},t)\frac{\partial U_\beta(\boldsymbol{x},t)}{\partial x_\alpha}\Big] &= i\int d^3q \int d^3q' q'_\beta U_\beta(\boldsymbol{q},t)U_\alpha(\boldsymbol{q}',t)\delta(\boldsymbol{q}+\boldsymbol{q}'-\boldsymbol{k}) \\ &= i\int d^3q (k_\beta - q_\beta)U_\beta(\boldsymbol{q},t)U_\alpha(\boldsymbol{k}-\boldsymbol{q},t) \\ &= ik_\beta \int d^3q\, U_\beta(\boldsymbol{q},t)U_\alpha(\boldsymbol{k}-\boldsymbol{q},t)\end{aligned} \tag{2.16}$$

Where we used 2.12 in the last line. For a more in depth derivation of this see [3]. This then leads to the Navier-Stokes equation in wavespace:

$$(\partial_t + \nu k^2)U_\alpha(\boldsymbol{k},t) + ik_\beta \int d^3q\, U_\beta(\boldsymbol{q},t)U_\alpha(\boldsymbol{k}-\boldsymbol{q},t) = \frac{k_\alpha}{i\rho}p(\boldsymbol{k},t) \tag{2.17}$$

We can eliminate the pressure term from 2.17 by taking the divergence of the equation and imposing the continuity condition (2.12), this gives:

$$\frac{k_\alpha k_\beta}{k^2}\int d^3q\, U_\beta(\boldsymbol{q},t)U_\alpha(\boldsymbol{k}-\boldsymbol{q},t) = -\frac{1}{\rho}p(\boldsymbol{k},t) \tag{2.18}$$

Then, by substituting back into the Fourier space Navier-Stokes equation 2.14 we get:

$$(\partial_t + \nu k^2)\, U_\alpha(\boldsymbol{k}, t) = -ik_\gamma \Big(\delta_{\alpha\beta} - \frac{k_\alpha k_\beta}{k^2}\Big) \int d^3q\, U_\gamma(\boldsymbol{q}, t)\, U_\beta(\boldsymbol{k} - \boldsymbol{q}, t)$$
$$(\partial_t + \nu k^2)\, U_\alpha(\boldsymbol{k}, t) = -ik_\gamma P_{\alpha\beta} \int d^3q\, U_\gamma(\boldsymbol{q}, t)\, U_\beta(\boldsymbol{k} - \boldsymbol{q}, t) \tag{2.19}$$

where we relabeled the dummy indices $\beta, \alpha \to \gamma, \beta$ for simplicity. $P_{\alpha\beta}$ is known as the projection operator, defined as:

$$P_{\alpha\beta} = \delta_{\alpha\beta} - \frac{k_\alpha k_\beta}{k^2} \tag{2.20}$$

The projection operator contains important properties that guarantee the velocity fields remains solenoidal, as it will remove from the velocity field any finite divergence. It is also appropriate, when needed, to define the Fourier transform of the forced Navier-Stokes equation, where we simply add the forcing term Fourier transform equivalent to 2.19:

$$(\partial_t + \nu k^2)\, U_\alpha(\boldsymbol{k}, t) = -ik_\gamma P_{\alpha\beta} \int d^3q\, U_\gamma(\boldsymbol{q}, t)\, U_\beta(\boldsymbol{k} - \boldsymbol{q}, t) + \boldsymbol{F}_k(\boldsymbol{k}, t) \tag{2.21}$$

2.1.3 The Vorticity Equation

It is also possible to eliminate the pressure through taking the curl of the Navier-Stokes equation. This method gives us a new quantity, vorticity, which is useful in describing the transfer of energy from low k values to high k values, e.g. the energy cascade.

We begin by defining vorticity: a pseudovector field that describes local spinning motion near a particular location in configuration space. The reference frame for vorticity is Lagrangian, e.g. at the point of measurement and flowing with the fluid. It is described mathematically by:

$$\boldsymbol{\omega} = \nabla \times \boldsymbol{U} \tag{2.22}$$

When taking the curl of the Navier Stokes equation (2.8) and utilizing the identity $\nabla U^2 = 2\boldsymbol{U} \cdot \nabla \boldsymbol{U} + 2\boldsymbol{U} \times (\boldsymbol{U} \times \boldsymbol{\omega})$, we get:

$$\partial_t \boldsymbol{\omega} = \nabla \times (\boldsymbol{U} \times \boldsymbol{\omega}) + \nu \nabla^2 \boldsymbol{\omega} \tag{2.23}$$

This is known as the *vorticity equation*, and in order to obtain 2.23 in terms of vorticity, we must solve 2.22 for velocity, $\boldsymbol{U}$. A similar process compared to our above FT can be used to solve the vorticity equation, and the same non-local operator appears. We can simplify 2.23 using the divergenceless natures of $\boldsymbol{\omega}$ and $\boldsymbol{U}$ through expanding:

$$\nabla \times (\boldsymbol{U} \times \boldsymbol{\omega}) = (\boldsymbol{\omega} \cdot \nabla)\boldsymbol{U} - (\boldsymbol{U} \cdot \nabla)\boldsymbol{\omega} + \boldsymbol{U}\nabla \cdot \boldsymbol{\omega} - \boldsymbol{\omega}\nabla \cdot \boldsymbol{U} \tag{2.24}$$

And since $\nabla \cdot \boldsymbol{U} = \nabla \cdot \boldsymbol{\omega} = 0$, hence:

$$\nabla \times (\boldsymbol{U} \times \boldsymbol{\omega}) = (\boldsymbol{\omega} \cdot \nabla)\boldsymbol{U} - (\boldsymbol{U} \cdot \nabla)\boldsymbol{\omega} \tag{2.25}$$

When injected back into the vorticity equation (2.23) we get:

$$\partial_t \boldsymbol{\omega} = (\boldsymbol{\omega} \cdot \nabla)\boldsymbol{U} - (\boldsymbol{U} \cdot \nabla)\boldsymbol{\omega} + \nu \nabla^2 \boldsymbol{\omega} \tag{2.26}$$

In this form it is easier to visualize what is happening over time. The time evolution of the vorticity is in terms of a 'stretching' term $(\boldsymbol{\omega} \cdot \nabla)\boldsymbol{U}$, 'diffusion' term $\nu \nabla^2 \boldsymbol{\omega}$, and 'advective' term $-(\boldsymbol{B} \cdot \nabla)\boldsymbol{\omega}$.

We will see later how vorticity is used to describe the energy cascade, where energy transfers to larger wavelengths in turbulent systems.

2.2 Kolmogorov Scales and the Energy Cascade

One issue of particular importance when building a simulation involving turbulence is the the scale in which the computations cut off at. Ideally this should be when kinetic energy is no longer cascading down in the form of eddies, the characteristic swirls that are seen in a river's flow or the eye of a hurricane. These eddies energetically cascade over time into smaller and smaller versions of themselves. The famous physicist and meteorologist Lewis Fry Richardson has a quote which greatly aids in the visualization of this energy cascade:

"Big whorls have little whorls that feed on their velocity,

and little whorls have lesser whorls and so on to viscosity."

There comes a certain point in which the kinetic energy involved in the swirling begins to dissipate into heat and dissipative forces take over, where turbulent effects are no longer of concern. This was first hypothesized by Kolmogorov in 1941 in his papers [2] and [11], and is effectively known as the Kolmogorov scale. In this section we briefly introduce his hypothesis and dissipation theory, ending with a quick overview on the mechanic of the energy cascade. For further reading, see: [12], [13], and [14].

2.2.1 Kolmogorov's Hypothesis

For the extent of this report, we solely use Direct Numerical Simulations for our results. DNS is advantageous because of its ability to iterate through all scales of configuration space, and we further expand upon this computational method in section 3. To begin, our simulation considers a cubical box sample size L, which can be associated with a velocity scale: $\Delta \boldsymbol{U}$ (the variation of the velocity over the distance of L). We initially consider the distance L as the system size, but can also consider the microscopic changes in velocity at much smaller configuration scales without loss of generality because of the nature of the energy cascade (where large eddies directly influence smaller eddies). At the scale of dissipation, the action of viscosity takes over, and kinetic energy then is converted to heat. We use this to define a dissipation rate as:

$$\varepsilon \approx \frac{(\Delta \boldsymbol{U})^3}{L} \tag{2.27}$$

This is our isotropic turbulence rate of dissipation. We utilize this parameter to obtain a scale at which dissipation begins to occur, namely the Kolmogorov microscale:

$$\xi = \left(\frac{\nu^3}{\varepsilon}\right)^{\frac{1}{4}} \tag{2.28}$$

Which can be used to depict the total number of degrees of freedom, N, of the whole system through:

$$N \approx \frac{L^3}{\xi^3} \tag{2.29}$$

So, in a numerical simulation, ξ is the smallest scale that should be resolved. Then, in $\boldsymbol{k}$ space, we can define the minimum k value k_{min}:

$$k_{min} = \frac{2\pi}{L_{max}} \tag{2.30}$$

Where L_{max} is the largest dimension used in the system. Small k values correspond to the largest scales in configuration space which, in turn, represents the largest eddies. In our simulations, we istropically force to the 2nd or 3rd wavenumber. We can then find the largest k number at the smallest scale in configuration space, the inverse of the Kolmogorov microscale (2.28):

$$k_{max} = \frac{1}{\xi} = \left(\frac{\varepsilon}{\nu^3}\right)^{\frac{1}{4}} \tag{2.31}$$

All scales smaller than ξ are called the *dissipation range*, and at ξ non-linear interactions are in equilibrium with viscous dissipative operations (all viscous effects are equal to turbulent effects) [13]. Kolmogorov then speculated [11] that at high Re, the energy spectrum within the inertial range ($L^{-1} < k < \xi^{-1}$) could then be defined as:

$$E(k) = \epsilon^{\frac{2}{3}} k^{-\frac{5}{3}} F(\xi k) \tag{2.32}$$

where $F(\xi k)$ is defined to be a dimensionless function.

In this high Re limit, Kolmogorov stated that through the relationship defined in eqn. 2.32, all small-scale statistical properties could be universally defined through the dissipation rate (ϵ), length scale (L), and the viscosity (ν). Then, in his second universality assumption, he defines the large Re limit for F found in eqn 2.32, such that:

$$F(\xi k) = \alpha(\xi k)^{-\frac{5}{3}} = \alpha \nu^{-\frac{5}{4}} \xi^{\frac{5}{12}} k^{-\frac{5}{3}} \tag{2.33}$$

For constant α. This leads into the *Kolmogorov five-thirds law* at large Re:

$$E(k) = \beta\epsilon^{\frac{2}{3}}k^{-\frac{5}{3}} \tag{2.34}$$

For dimensionless constant β, this rule states that when our system is largely turbulent, we should expect to see a dissipation rate dependent power law for k in the energy spectra. The energy spectrum is explicitly outlined in the next section. This, however, is for hydrodynamics and certain important arguments have been made that suggests a different spectrum being seen in MHD. We discuss this in section 2.3.3.

2.2.2 The Energy Cascade and Transfer Functions

Energy transfer over time is important for understanding the behaviour of isotropic turbulence. It is possible to derive a spectral representation of energy, the value at each wavenumber in this spectra indicates the amount of energy contained in the system at that particular value of k. This in turn allows for us to determine the energetic transfer at any length scale. A fundamental representation for this energy spectrum is derived. In this derivation we note another important quantity, the Transfer Function, which gives the amount of energy transferring between different length scales (or wavenumbers) at any instance of time. See [3] for a more in-depth derivation described in this section.

When systems of numerous points are simulated in computational fluid dynamics (CFD), each point has their own velocity/magnetic field quantities; this requires the usage of statistics to build total magnetic and kinetic energies. We do this through defining the systemic energy density by:

$$E(t) = \frac{1}{2}\langle|\boldsymbol{U}(\boldsymbol{x},t)|^2\rangle \tag{2.35}$$

Taking the Fourier transform, and noting that our velocity field is real (i.e. $\boldsymbol{U}^*(\boldsymbol{k}) = \boldsymbol{U}(-\boldsymbol{k})$) we arrive at:

$$E(\boldsymbol{x},t) = \frac{1}{2}\int d^3\boldsymbol{k}\langle\boldsymbol{U}(\boldsymbol{k},t)\boldsymbol{U}(-\boldsymbol{k},t)\rangle = \frac{1}{2}\int dk\, k^2\int_\Omega d\Omega\langle|\boldsymbol{U}(\boldsymbol{k},t)|^2\rangle \tag{2.36}$$

where $d\Omega$ is the differential solid angle in spherical coordinates and $\langle\ \rangle$ the mean of all velocity states (i.e. the ensemble average). This allows us to define spectra of energy in Fourier space:

$$E(\boldsymbol{k},t) = \frac{k^2}{2}\int_\Omega d\Omega\langle|\boldsymbol{U}(\boldsymbol{k},t)|^2\rangle \tag{2.37}$$

A temporal progression can be defined for our energy spectrum when we take the ensemble averages of the left sided product with the opposite Fourier mode $(-\boldsymbol{k})$ of 2.9:

$$\langle U_\alpha(-\boldsymbol{k},t)(\partial_t+\nu^2k^2)\,U_\alpha(\boldsymbol{k},t)\rangle = M_{\alpha\beta\gamma}(\boldsymbol{k})\int d^3q\langle U_\alpha(-\boldsymbol{k},t)\,U_\beta(\boldsymbol{q},t)\,U_\gamma(\boldsymbol{k}-\boldsymbol{q},t)\rangle \\ +\langle U_\alpha(-\boldsymbol{k},t)F_\alpha(\boldsymbol{k},t)\rangle \tag{2.38}$$

and we consider the opposite case, for the sake of symmetry:

$$\langle U_\alpha(\boldsymbol{k},t)(\partial_t+\nu^2k^2)\,U_\alpha(-\boldsymbol{k},t)\rangle = M_{\alpha\beta\gamma}(-\boldsymbol{k})\int d^3q\langle U_\alpha(\boldsymbol{k},t)\,U_\beta(\boldsymbol{q},t)\,U_\gamma(-\boldsymbol{k}-\boldsymbol{q},t)\rangle \\ +\langle U_\alpha(\boldsymbol{k},t)F_\alpha(-\boldsymbol{k},t)\rangle \tag{2.39}$$

where $M_{\alpha\beta\gamma}$ is the symmetric vertex operator, defined over all space by:

$$M_{\alpha\beta\gamma}(\boldsymbol{k}) = \frac{1}{2i}\Big(k_\gamma P_{\alpha\beta} + k_\beta P_{\alpha\gamma}\Big) \tag{2.40}$$

Adding 2.38 and 2.39 and assuming all equal times (i.e. ignoring time dependence) we arrive at:

$$(\partial_t+\nu^2k^2)\langle U_\alpha(-\boldsymbol{k})\,U_\alpha(\boldsymbol{k})\rangle = M_{\alpha\beta\gamma}(\boldsymbol{k})\int d^3q\langle U_\alpha(-\boldsymbol{k})\,U_\beta(\boldsymbol{q})\,U_\gamma(\boldsymbol{k}-\boldsymbol{q})\rangle \\ +M_{\alpha\beta\gamma}(-\boldsymbol{k})\int d^3q\langle U_\alpha(\boldsymbol{k})\,U_\beta(\boldsymbol{q})\,U_\gamma(-\boldsymbol{k}-\boldsymbol{q})\rangle \\ +\langle U_\alpha(-\boldsymbol{k})F_\alpha(\boldsymbol{k})\rangle + \langle U_\alpha(\boldsymbol{k})F_\alpha(-\boldsymbol{k})\rangle \tag{2.41}$$

This is simplified by relating the RHS quantities through conjugation, such that: $U_\alpha(-\boldsymbol{k}) = U_\alpha^*(\boldsymbol{k})$ and $M_{\alpha\beta\gamma}(-\boldsymbol{k}) = M^*_{\alpha\beta\gamma}(\boldsymbol{k})$. This gives:

$$(\partial_t+\nu^2k^2)\langle U_\alpha(-\boldsymbol{k})\,U_\alpha(\boldsymbol{k})\rangle = 2Re\Big[M_{\alpha\beta\gamma}(\boldsymbol{k})\int d^3q\langle U_\alpha(-\boldsymbol{k})\,U_\beta(\boldsymbol{q})\,U_\gamma(\boldsymbol{k}-\boldsymbol{q})\rangle\Big] \\ +\ 2Re[\langle F_\alpha(\boldsymbol{k})\,U_\alpha(-\boldsymbol{k})\rangle] \tag{2.42}$$

Where the first term on the RHS can be defined as the transfer spectrum:

$$T(k,t) = 4\pi k^2 T(\boldsymbol{k}) = Re\Big[M_{\alpha\beta\gamma}(\boldsymbol{k})\int d^3q\langle U_\alpha(-\boldsymbol{k})\,U_\beta(\boldsymbol{q})\,U_\gamma(\boldsymbol{k}-\boldsymbol{q})\rangle\Big] \tag{2.43}$$

We assume isotropy and homogeneity, this allows us to simplify 2.42 and derive the *Lin Equation:*

$$\partial_t E(k) + D(k) = T(k) + W(k) \tag{2.44}$$

This equation describes the time evolution of the energy spectrum at any Fourier mode k through the sum of three different spectra: $D(k, \mathrm{t}) \sim$ the dissipation term, $T(k, \mathrm{t}) \sim$ the transferm spectrum (2.43), and $W(k, \mathrm{t}) \sim$ the work spectrum. We may interpret 2.44 as the change in energy being equal to the amount of energy forced in and/or transferred in minus the amount dissipating out.

The Transfer Function allows us to interpret how the energy is moving in between different wavenumbers in spectral space. It has been seen in HD that self-organized flows, such as Beltrami states, show the transfer function is zero across all k values [24].

2.3 Extension to Magnetohydrodynamics

2.3.1 MHD Equations

If a fluid is electrically conductive, our hydrodynamic Navier-Stokes equation can no longer describe everything that happens in the system. We must resort to the MHD equations, which take into account the magnetic phenomena that occur as the fluid churns and flows. A deeper insight and extrapolation of what is discussed in this section can be found in [16]. Turbulent salt water or liquid metal in a planet's core are two examples of an MHD system, and we describe the dynamics of such through the following laws:

$$\partial_t \boldsymbol{U} = -(\boldsymbol{U} \cdot \nabla)\boldsymbol{U} - \frac{1}{\rho}\nabla p + \nu(\nabla^2 \boldsymbol{U}) + \frac{1}{\rho}(\nabla \times \boldsymbol{B}) \times \boldsymbol{B} \tag{2.45}$$

$$\partial_t \boldsymbol{B} = (\boldsymbol{B} \cdot \nabla)\boldsymbol{U} - (\boldsymbol{U} \cdot \nabla)\boldsymbol{B} + \eta\nabla^2 \boldsymbol{B} \tag{2.46}$$

$$\nabla \cdot \boldsymbol{U} = 0 \tag{2.47}$$

$$\nabla \cdot \boldsymbol{B} = 0 \tag{2.48}$$

Where $\boldsymbol{U}$ defines the fluid velocity, ρ the density, p the systemic isothermal pressure, ν the viscosity, and $\boldsymbol{B}$ the induced magnetic field.

The first equation describes the change in the fluid velocity over time, where the only diffference between the HD Navier-Stokes equation is the end Lorentz force term on the right side. Eq. 2.46 is called the Induction Equation, and reflects the time evolution of the magnetic field (this is comparable to the vorticity equation in HD, eqn. 2.23). The final two quantities 2.47 and 2.48 give conservation of mass and require $\boldsymbol{B}$ to be divergenceless. These equations describe the nature of conductive fluids, conservation laws, and define the dynamics of $\boldsymbol{B}$ and its interaction with the fluid. If we were to simulate them as is with a set initial amount of energy, the energy would quickly decay away (as discussed in prior sections) [17]. One would need to force the system energetically in order to maintain a steady state, this is done through adding a forcing term to 2.45 and 2.46.

Though the MHD equations have already been presented, we will derive both eqn. 2.45 and eqn. 2.46 for the sake of clarity in the first two sub-sections. These processes will be in a similar fashion to the derivation of the N-S and Vorticity equations, but with added depth.

2.3.2 Derivation of the MHD Equations

We begin by deriving the equation of motion (2.45) through considering the forces that are actively working on a fluid element, δV and the element's mass differential: $\rho\delta V$, where ρ is the corresponding mass density. A similar process can be used to derive the N-S eqn. 2.2, which we did not choose to do as our report solely focuses on MHD.

The three forces are:

1. **The Lorentz Force ($F_{\boldsymbol{L}}$)**: In an electromagnetic field $\boldsymbol{E}$, $\boldsymbol{B}$ the $i^{\,th}$ particle of charge q_i is subject to the Lorentz Force $q_i(\boldsymbol{E} + \boldsymbol{U}_i \times \boldsymbol{B}/c)$. We consider the notion that macroscopically, a fluid element is dependent upon the forces acting on the individual particles that comprise this element. Therefore, we write: $\delta q\boldsymbol{E} + \delta\boldsymbol{J} \times \boldsymbol{B}/c$ for the differential electric current carried by the fluid element, $\delta\boldsymbol{J}$. By quasi-neutrality we assume $\delta q \simeq 0$, where the field isn't vanishing here, but on macroscopic scales electrostatic fields enforce charge neutrality. This leaves the magnetic part of the Lorentz force to be equal to:

$$\delta V\frac{1}{c}\boldsymbol{j} \times \boldsymbol{B} \tag{2.49}$$

   where we can rewrite $\delta V\boldsymbol{j}$ as $\delta\boldsymbol{J}$, with $\boldsymbol{j}$ being the current density.

2. **Thermal Pressure Force ($F_{\boldsymbol{P}}$)**:

   With the assumption that our system is close to local thermodynamic equilibrium, we can say the pressure tensor is isotropic, i.e. $p_{ij} = p\delta_{ij}$. This gives a force:

$$-\oint p d\boldsymbol{S} = -\delta V\nabla p \tag{2.50}$$

   and the integral is over the surface of the fluid element.

3. **The Viscous Force (F_{ν})**:

   This force is similar to the pressure force, and acts within the volume of the fluid element rather than over just the surface area:

$$\oint \boldsymbol{\sigma}^{(ij)} \cdot d\ \boldsymbol{S} = \delta V\nabla \cdot \boldsymbol{\sigma^{(\nu)}} \tag{2.51}$$

   where $\boldsymbol{\sigma}^{(\nu)} = \{\sigma_{ij}^{(\nu)}\}$ is the viscous stress tensor:

$$\sigma_{ij}^{(\nu)} = \nu[(\partial_i U_j + \partial_j U_i) - \frac{2}{3}\delta_{ij}\nabla \cdot \boldsymbol{U}] \tag{2.52}$$

and ν is the viscosity, assumed constant. Note that as our fluid is assumed to be incompressible, we may disregard the second term for the stress tensor ($\nabla \cdot \boldsymbol{U} = 0$).

Since our fluid is continuously deforming, it is important to use the material or Lagrangian derivative when defining our momentum equation:

$$\frac{D\boldsymbol{U}}{dt} = (\partial_t + \boldsymbol{U} \cdot \nabla)\boldsymbol{U} \tag{2.53}$$

Then, disregarding effects of gravity, by Newton's Second Law:

$$\rho\frac{D\boldsymbol{U}}{dt} = F_\nu + F_L + F_V \tag{2.54}$$

which gives the equation:

$$\rho\frac{D\boldsymbol{U}}{dt} = \rho(\partial_t + \boldsymbol{U} \cdot \nabla)\boldsymbol{U} = -\nabla p + \frac{1}{c}\boldsymbol{j} \times \boldsymbol{B} + \nu(\nabla^2\boldsymbol{U} + \frac{1}{3}\nabla(\nabla \cdot \boldsymbol{U})) \tag{2.55}$$

Where on the right hand side we used the definition of the viscous stress tensor, $\boldsymbol{\sigma}^{(\nu)}$ and took the divergence (as seen in the Viscous Force definition above):

$$\partial_i\sigma_{ij}^{(\nu)} = \nu\partial_i[(\partial_i U_j + \partial_j U_i)] = \nu(\nabla^2\boldsymbol{U} + \nabla(\nabla \cdot \boldsymbol{U})) \tag{2.56}$$

By conservation of mass the second term vanishes ($\nabla \cdot \boldsymbol{U} = 0$). To simplify the term with current density, $\boldsymbol{j}$, we use Ampere's Law:

$$\nabla \times \boldsymbol{B} = \frac{4\pi}{c}\boldsymbol{j} \tag{2.57}$$

and substitute into the above $1/c$ ($\boldsymbol{j} \times \boldsymbol{B}$) term, leaving eq. 2.55 solely reliant on the induced magnetic field ($\boldsymbol{B}$) and the fluid velocity ($\boldsymbol{U}$):

$$\frac{D\boldsymbol{U}}{dt} = -\frac{1}{\rho}\nabla p + \frac{1}{\rho}(\nabla \times \boldsymbol{B}) \times \boldsymbol{B} + \nu(\nabla^2\boldsymbol{U}) \tag{2.58}$$

or

$$\partial_t\boldsymbol{U} = -\boldsymbol{U}(\boldsymbol{U} \cdot \nabla) - \frac{1}{\rho}\nabla p + \frac{1}{\rho}(\nabla \times \boldsymbol{B}) \times \boldsymbol{B} + \nu(\nabla^2\boldsymbol{U}) \tag{2.59}$$

This is the equation of motion for our MHD turbulent fluid; as stated, the only change from our hydrodynamic Navier-Stokes equation is the Lorentz Force term, $\frac{1}{\rho}(\nabla \times \boldsymbol{B}) \times \boldsymbol{B}$.

2.3.3 The Induction Equation

To determine the time evolution of the magnetic field, $\boldsymbol{B}$, we utilize Faraday's Law:

$$\partial_t \boldsymbol{B} = -c\nabla \times \boldsymbol{E} \tag{2.60}$$

We consider the rest frame of the fluid element and define $\boldsymbol{E}$ to be: $\boldsymbol{E} = \boldsymbol{j}/\sigma$, where σ is the electrical conductivity. In the lab frame, a fluid element is moving at velocity $\boldsymbol{U}$ and we can perform the transformation:

$$\boldsymbol{E} \rightarrow \boldsymbol{E'} = \boldsymbol{E} + \boldsymbol{U} \times \boldsymbol{B}/c \tag{2.61}$$

This allows us to create the generalized version of Ohm's law (for a moving conductive fluid):

$$\boldsymbol{E} + \frac{1}{c}\boldsymbol{U} \times \boldsymbol{B} = \frac{1}{\sigma}\boldsymbol{j} \tag{2.62}$$

Substituting back into Faraday's Law (2.60) and assuming uniform conductivity yields the induction equation:

$$\partial_t \boldsymbol{B} - \nabla \times (\boldsymbol{U} \times \boldsymbol{B}) = \eta \nabla^2 \boldsymbol{B} \tag{2.63}$$

Where $\eta = c^2/4\pi\sigma$ is the magnetic diffusivity. This equation defines the behaviour of the magnetic field. With the identity:

$$\nabla \times (\boldsymbol{A} \times \boldsymbol{B}) = \boldsymbol{A}(\nabla \cdot \boldsymbol{B}) - \boldsymbol{B}(\nabla \cdot \boldsymbol{A}) + (\boldsymbol{B} \cdot \nabla)\boldsymbol{A} - (\boldsymbol{A} \cdot \nabla)\boldsymbol{B} \tag{2.64}$$

and eqns. 2.47 and 2.48, we can rewrite 2.63 as the Induction Equation:

$$\partial_t \boldsymbol{B} = (\boldsymbol{B} \cdot \nabla)\boldsymbol{U} - (\boldsymbol{U} \cdot \nabla)\boldsymbol{B} + \eta \nabla^2 \boldsymbol{B} \tag{2.65}$$

The $(\boldsymbol{B} \cdot \nabla)\boldsymbol{U}$ term in the above form of the Induction Equation describes how the magnetic field lines stretch with the flow of the liquid and is responsible for the transfer of magnetic energy to kinetic energy. The $\eta\nabla^2\boldsymbol{B}$ corresponds to the magnetic dissipation, and $-(\boldsymbol{U} \cdot \nabla)\boldsymbol{B}$ is responsible for the redistribution of magnetic energy.

This concludes the derivation of the two MHD equations, which are used by our simulation software to solve for fluctuations in the fluid velocity ($\boldsymbol{U}$) and magnetic field ($\boldsymbol{B}$) at many different points. We will see (in a similar fashion to section 2.17) in section 2.3.6 how they are transformed to spectral space. In section 2.3.5 we describe how these equations are energetically forced to sustain a turbulent spectrum over a period of time.

The Magnetic Reynolds Number

If we consider the magnetic properties of turbulence, it's often helpful to define a second quantity: the Magnetic Reynolds Number:

$$Re_m = \frac{\boldsymbol{U}l}{\eta} \tag{2.66}$$

Where the only thing that changes from the hydrodynamic Reynolds number is the usage of η, the magnetic diffusivity.

Prandtl Number

In MHD systems, both the hydrodynamic and magnetic parts interlock and influence each other via different mechanisms such as the dynamo effect (where kinetic energy is converted into magnetic energy). It's convenient to use the Prandtl number, which takes the ratio of Re_m and Re, resulting in simple a ratio of the kinematic viscosity and magnetic diffusivity of the fluid:

$$Pr_m = \frac{Re_m}{Re} = \frac{\nu}{\eta} \tag{2.67}$$

The Prandtl number helps us realize how important the magnetic effects are on a particular system; For $Pr \ll 1$ the viscous effects define the turbulent progression of a fluid, and for $Pr \gg 1$ the magnetic effects dominate.

For the results posted in this report, we choose to have a Prandtl number equal to 1 (that is, identical Re and Re_m values), as it is common in most MHD simulations to do so for the sake of simplicity. This ensures one property (such as the magnetic field) of the system won't be dominant over the other.

MHD Power Law

Here we briefly extend the end portion of section 2.2.1 to MHD. As stated, the Kolmogorov 5/3 law is defined in the large (but not infinite) Re limit for HD as:

$$E(k) = \beta \epsilon^{\frac{2}{3}} k^{-\frac{5}{3}} \tag{2.68}$$

For a dimensionless constant β. In the early 1960s, however, it was shown that the added presence of a magnetic field energetically dampened the system's energy transfer between different wavenumbers [18] [19]. This lead to a new speculated spectrum for MHD defined as:

$$E(k) \propto k^{-\frac{3}{2}} \tag{2.69}$$

which is the Iroshnikov-Kraichnan (IK) spectrum. In our results (section 4.1.4) we hope to find a similarity between eqn. 2.69 and the behaviours of our simulated energy spectra.

2.3.4 Ideal Conserved Quantities in MHD

Three important quantities in MHD are observed to be conserved in the ideal limit where dissipation and forcing become absent: *energy*, *magnetic helicity*, and *cross helicity*. We wish to see if the behaviours of these quantities have an effect on one another, and any possible correlations are investigated in section 4.1.3 of our results. Helicity is defined by a measure of how tangled or linked certain vector field lines are in the dynamical system. Total energy consists of the kinetic (where the fluid is moving around) and the magnetic (caused by the induced magnetic field) added together. Interactions between widely separated scales in MHD are more important than in HD, as large scale magnetic energy can equally be influenced by smaller scales of kinetic and magnetic interaction /helicity through the *Alfvén Effect* [20]. We present in this section the conservation behaviour of these quantities in the limit where the system is without dissipation. In other words, when a steady state MHD homogeneous isotropic turbulence energy is added at the same rate it is lost through dissipation. For more information on the conservation proofs found in this section, see [21].

Energy Conservation

We begin by showing the conservation equation for the MHD system's total energy, found through taking the scalar product of momentum ($\rho\boldsymbol{U}$) with 2.45 and $\boldsymbol{B}$ with 2.63 then adding them together to produce a rate of change for total energy, E_T. Using the identities:

$$\boldsymbol{B}\cdot(\nabla\times(\boldsymbol{U}\times\boldsymbol{B})) = -\nabla\cdot(\boldsymbol{B}\times(\boldsymbol{U}\times\boldsymbol{B})) + \boldsymbol{U}\times\boldsymbol{B}\cdot\boldsymbol{j} \tag{2.70}$$

$$\boldsymbol{U}\cdot(\boldsymbol{j}\times\boldsymbol{B}) = \boldsymbol{j}\cdot(\boldsymbol{U}\times\boldsymbol{B}) \tag{2.71}$$

$$\nu\nabla^2\boldsymbol{U}\cdot\boldsymbol{U} = \nu(\nabla\times\boldsymbol{U})^2 = \nu\boldsymbol{\omega}^2 \tag{2.72}$$

$$\eta\nabla^2\boldsymbol{B}\cdot\boldsymbol{B} = (1/\sigma)j^{\,2} \tag{2.73}$$

we take the first product of $\rho\boldsymbol{U}$ with the equation of motion for MHD (2.45):

$$\rho\boldsymbol{U}\cdot\partial_t\boldsymbol{U} = \frac{\rho}{2}\partial_t\boldsymbol{U}^2 = -\rho\boldsymbol{U}\cdot(\boldsymbol{U}\cdot\nabla)\boldsymbol{U} - \boldsymbol{U}\cdot\nabla p + \nu\nabla^2\boldsymbol{U}\cdot\boldsymbol{U} + \boldsymbol{U}\cdot((\nabla\times\boldsymbol{B})\times\boldsymbol{B}) \tag{2.74}$$

and the second product of $\boldsymbol{B}$ with the induction equation 2.46 gives:

$$\boldsymbol{B}\cdot\partial_t\boldsymbol{B} = \frac{1}{2}\partial_t\boldsymbol{B}^2 = \boldsymbol{B}\cdot(\nabla\times(\boldsymbol{U}\times\boldsymbol{B})) + \eta\nabla^2\boldsymbol{B}\cdot\boldsymbol{B} \tag{2.75}$$

With 2.74, 2.75 and the above defined identities, we add together to form:

$$\frac{1}{2}\,\partial_t(\rho\boldsymbol{U}^2+\boldsymbol{B}^2) = -\nabla\cdot\left[\frac{\rho}{2}\boldsymbol{U}^2+p\right]\boldsymbol{U} - \nabla\cdot(\boldsymbol{B}\times(\boldsymbol{U}\times\boldsymbol{B})) + \frac{1}{\sigma}\boldsymbol{j}^2 + \nu\boldsymbol{\omega}^2 \tag{2.76}$$

We now have an identity that involves the magnetic and kinetic energy densities, hence integrating over all space gives us the total system energy. This quantity we frequently visit when investigating simulation results, as it reveals the overall behaviour of turbulence in the system and when we arrive at a steady, isotropically turbulent state. Taking the volumetric integral over all space gives:

$$\frac{1}{2}\partial_t \int_V (\rho \boldsymbol{U}^2 + \boldsymbol{B}^2) dV = \int_V \left[-\nabla \cdot \left[\frac{\rho}{2} \boldsymbol{U}^2 + p \right] \boldsymbol{U} - \nabla \cdot (\boldsymbol{B} \times (\boldsymbol{U} \times \boldsymbol{B})) + \frac{1}{\sigma} \boldsymbol{j}^2 + \nu \boldsymbol{\omega}^2 \right] dV \quad (2.77)$$

We use the divergence theorem to reduce the two volumetric integrals in the first portion of the RHS to derive a surface integral:

$$\frac{1}{2}\partial_t \int_V (\rho \boldsymbol{U}^2 + \boldsymbol{B}^2) dV = -\int_S \left[\left(\frac{\rho}{2} \boldsymbol{U}^2 + p \right) \boldsymbol{U} + (\boldsymbol{B} \times (\boldsymbol{U} \times \boldsymbol{B})) \right] \cdot \hat{\mathbf{n}} \, dS + \int_V \left(\frac{1}{\sigma} \boldsymbol{j}^2 + \nu \boldsymbol{\omega}^2 \right) dV \quad (2.78)$$

The surface integral represents the energy flux and the volume integral represents the system's energy dissipation. Therefore, in the non-dissipation limit of the total energy's rate of change, e.g. $\partial_t E_T = 0$, the energetic flux is equal to the dissipation:

$$\int_S \left[\left(\frac{\rho}{2} \boldsymbol{U}^2 + p \right) \boldsymbol{U} + (\boldsymbol{B} \times (\boldsymbol{U} \times \boldsymbol{B})) \right] \cdot \hat{\mathbf{n}} \, dS = \int_V \left(\frac{1}{\sigma} \boldsymbol{j}^2 + \nu \boldsymbol{\omega}^2 \right) dV \quad (2.79)$$

or

$$\int_S \boldsymbol{F}_E \cdot \hat{\mathbf{n}} \, dS = D_E \quad (2.80)$$

And energy is conserved, this then would be a steady state of turbulence, and in our results we investigate different quantitative traits (such as energy spectra and helicities) found in such states.

Helicities

In MHD systems, we consider two helical quantities: cross and magnetic. These correspond to the added magnetic effects that happen in MHD and how the magnetic field lines tangle and knot with each other and the fluid's velocity. We also mention a third quanitity, kinetic helicity, though this is only looked at in HD.

In greater detail, these different helicities are defined as:

1. **Kinetic Helicity:**

$$H_k = \int_V d^3\boldsymbol{x} \, \boldsymbol{U} \cdot \boldsymbol{\omega} \quad (2.81)$$

   Where $\boldsymbol{\omega}$ is the vorticity defined in 2.22, and $\boldsymbol{U}$ the fluid velocity. This quantity measures the twisting and knotting of vortex tubes in the fluid (i.e. the voriticity itself) in hydrodynamic systems. Investigating its behaviour in MHD simulations has been done before, as it's been found that a non-zero kinetic helicity in the field is the cause for effects like kinematic dynamo, when there's a lack of reflectional symmetry in the velocity field, $\boldsymbol{U}$ [22]. In other words, the presence of kinetic helicity implies the velocity field lacks reflectional invariance [20]. Kinetic helicity is not conserved in MHD systems, however, due to the Lorentz force term found in 2.45; thus we solely consider the magnetic and cross helicities in our results.

2. **Magnetic Helicity:**

$$H_b = \int_V d^3\boldsymbol{x}\,\boldsymbol{A}\cdot\boldsymbol{B} \tag{2.82}$$

Where $\boldsymbol{A}$ is the magnetic vector potential, through Maxwell's laws its curl defines the magnetic field: $\boldsymbol{B} = \nabla\times\boldsymbol{A}$. Compared to kinetic helicity, magnetic helicity (MH) would be the MHD equivalent and is the measure of the linkage and entanglement of the magnetic field lines. Though the magnetic field, $\boldsymbol{B}$, is divergenceless (2.48), we can show the conservation of the magnetic helicity through taking the time derivative of 2.82. Showing conservation of the magnetic and cross helicity (introduced in the next list item) has a topological interpretation such that the number of infinitesimally sized flux tubes in our system remains constant over time [4].

We show conservation of magnetic helicity through:

$$\frac{dH_b}{dt} = \int_V d^3\boldsymbol{x}\Big[\boldsymbol{A}\cdot\frac{\partial\boldsymbol{B}}{\partial t} + \frac{\partial\boldsymbol{A}}{\partial t}\cdot\boldsymbol{B}\Big] + \boldsymbol{A}\cdot\boldsymbol{B}\frac{d}{dt}dV \tag{2.83}$$

We integrate the final term because our sample volume, dV, is moving with the fluid. This can be eliminated by evaluating the time derivative explicitly:

$$\frac{d}{dt}dV = \frac{d}{dt}dx_1dx_2dx_3 = V_1dx_2dx_3 + V_2dx_1dx_3 + V_3dx_1dx_2 = \mathbf{V}\cdot\hat{\mathbf{n}}\;dS \tag{2.84}$$

Which converts our volumetric integral into a simpler integral over the surface of the flux tube. As $\mathbf{V}\cdot\hat{\mathbf{n}}$ vanishes on the surface, the integral simply reduces to zero and we are left with the following from 2.83:

$$\frac{dH_b}{dt} = \int_V d^3\boldsymbol{x}\Big[\boldsymbol{A}\cdot\frac{\partial\boldsymbol{B}}{\partial t} + \frac{\partial\boldsymbol{A}}{\partial t}\cdot\boldsymbol{B}\Big] \tag{2.85}$$

Through choosing a specific gauge, namely: $\boldsymbol{E} = -\frac{1}{c}\frac{\partial\boldsymbol{A}}{\partial t}$, and choosing our vector potential, ϕ, be equal to zero:

$$\phi = \int_S \boldsymbol{B}\cdot\hat{\mathbf{n}}\;dS = 0 \tag{2.86}$$

we can begin to evaluate 2.83 through Faraday's Law:

$$\frac{dH_b}{dt} = c\int_V(-\boldsymbol{E}+\nabla\phi)\cdot\boldsymbol{B}dV + c\int_V\boldsymbol{A}\cdot(-\nabla\times\boldsymbol{E})\cdot\boldsymbol{B}dV \tag{2.87}$$

and since $\phi = 0$, we have:

$$\frac{dH_b}{dt} = -c\int_V \boldsymbol{E}\cdot\boldsymbol{B}dV + c\int_V \boldsymbol{A}\cdot(-\nabla\times\boldsymbol{E})\cdot\boldsymbol{B}dV \tag{2.88}$$

Now we use the identity $-\boldsymbol{A}\cdot(\nabla\times\boldsymbol{E}) = \nabla\cdot(\boldsymbol{A}\times\boldsymbol{E}) - \boldsymbol{E}\cdot(\nabla\times\boldsymbol{A})$ in 2.88:

$$\begin{aligned}\frac{dH_b}{dt} &= -c\int_V \Big[\boldsymbol{E}\cdot\boldsymbol{B} - \nabla\cdot(\boldsymbol{A}\times\boldsymbol{E}) + \boldsymbol{E}\cdot(\nabla\times\boldsymbol{A})\Big]dV \\ &= -2c\int_V \boldsymbol{E}\cdot\boldsymbol{B}dV + c\int_V \nabla\cdot(\boldsymbol{A}\times\boldsymbol{B})dV \\ &= -2c\int_V \boldsymbol{E}\cdot\boldsymbol{B}dV + c\int_S (\boldsymbol{A}\times\boldsymbol{E})\cdot\hat{\mathbf{n}}\;dS \\ &= -\frac{2c}{\sigma}\int_V \boldsymbol{j}\cdot\boldsymbol{B}\;dV\end{aligned} \tag{2.89}$$

Where in the second to last step we used the Divergence Theorem, and σ is the electrical conductivity from our definition of $\boldsymbol{E} = \boldsymbol{j}/\sigma$ by Ohm's law. In the dissipationless limit, $\eta \to 0$ (i.e. our dissipation term in eqn. 2.46 goes to 0), giving $\sigma \to \infty$, $\partial_t H_b \to 0$; thus showing conservation of magnetic helicity.

3. **Cross Helicity:**

Cross helicity (CH) is the second counterpart to magnetic helicity in MHD turbulence, and takes into account the interaction and knottedness of the fluid's flow velocity and magnetic field:

$$H_C = \int_V \boldsymbol{U}\cdot\boldsymbol{B}d^3\boldsymbol{x} \tag{2.90}$$

We can show it's conservation again by taking its time derivative, using 2.84 and assuming no dissipation:

$$\begin{aligned}\frac{dH_C}{dt} &= \int_V \Big[\boldsymbol{B}\cdot\frac{\partial\boldsymbol{U}}{\partial t} + \boldsymbol{U}\cdot\frac{\partial\boldsymbol{B}}{\partial t}\Big]dV \\ &= \int_V \Big[\boldsymbol{B}\cdot\Big(-(\mathbf{U}\cdot\nabla)\boldsymbol{U} - \frac{1}{\rho}\nabla p + \frac{1}{\rho}(\boldsymbol{j}\times\boldsymbol{B})\Big) + \boldsymbol{U}\cdot(\nabla\times(\boldsymbol{U}\times\boldsymbol{B}))\Big]dV\end{aligned} \tag{2.91}$$

Where in the second step we used 2.45 and 2.63 to substitute for the two time derivatives of the magnetic and velocity fields. The third term in 2.91 vanishes, and by assuming the adiabatic law $p \approx \rho^\Gamma$, we alter the second term (recall $\nabla\cdot\boldsymbol{B} = 0$) to:

$$\frac{1}{\rho}\boldsymbol{B}\cdot\nabla p = \nabla\cdot\Big(\frac{\Gamma}{\Gamma-1}\frac{p}{\rho}\boldsymbol{B}\Big) \tag{2.92}$$

where Γ is the adiabatic index ($\Gamma = 5/3$ for an ideal plasma) given through the ideal gas law (energy only depends on the pressure found in the system):

$$\rho E_T = \frac{p}{\Gamma - 1} \tag{2.93}$$

Using the identities:

$$\begin{aligned} \boldsymbol{U} \cdot \nabla \boldsymbol{U} &= \nabla(U^2/2) - \boldsymbol{U} \times \nabla \times \boldsymbol{U} \\ \boldsymbol{U} \cdot \nabla \times (\boldsymbol{U} \times \boldsymbol{B}) &= \nabla \cdot [\boldsymbol{U} \times (\boldsymbol{U} \times \boldsymbol{B})] + (\boldsymbol{U} \times \boldsymbol{B}) \cdot \nabla \times \boldsymbol{U} \end{aligned} \tag{2.94}$$

we combine the first and last terms in 2.91 to give a divergence:

$$-\boldsymbol{B} \cdot (\boldsymbol{U} \cdot \nabla \boldsymbol{U}) + \boldsymbol{U} \cdot \nabla \times (\boldsymbol{U} \times \boldsymbol{B}) = -\nabla \cdot \left[\frac{1}{2} U^2 \boldsymbol{B} - \boldsymbol{U} \times (\boldsymbol{U} \times \boldsymbol{B})\right] \tag{2.95}$$

Which, through using the divergence theorem we create a surface integral, giving us:

$$\frac{dH_C}{dt} = -\oint_S \hat{\mathbf{n}} \cdot \left[\left(\frac{1}{2} U^2 + \frac{\Gamma}{\Gamma - 1} \frac{p}{\rho}\right) \boldsymbol{B} - \boldsymbol{U} \times (\boldsymbol{U} \times \boldsymbol{B})\right] dS \tag{2.96}$$

When on the boundary S, the above quantity vanishes through the relations $\hat{\mathbf{n}} \cdot \boldsymbol{B} = \hat{\mathbf{n}} \cdot \boldsymbol{U} = 0$. This shows that the cross helicity is a fundamental conserved quantity in our MHD system.

A buildup in cross helicity with MHD systems has been observed at small simulation times (~ 60 seconds) and small Re [9]. Their results show it is difficult to tell whether the helicities are in a state of fluctuation, or actually accumulating over time. In our results we discuss and investigate these quantities at longer system times in an attempt to show whether or not they are simple fluctuations. All simulations we analyze begin with all helicity values at zero, but become finite over time due to different alignments and fluctuations from the fields.

2.3.5 Universality and Forcing the MHD Equations

In MHD there has been a large search to clarify the universality of MHD, i.e. the non-linear nature of how magnetohydrodynamics develop should have a predictable outcome - regardless of certain initial system traits and conditions. This began with Komogorov in 1941 with HD, where large-scale asymmetrical geometry had little to no effect on the symmetry found near the dissipation scales. The nature of MHD's universality, however, has recently been questioned, one example was made through the investigation of dissipation constant behaviours found in MHD decaying systems that start with differing values of helicity [23]. Their study indicated that at large Re, dissipation behaved dissimilarly between different systems of ranging values in cross and magnetic helicity. This presents a problem in the universality or prediction of how the MHD's large Re behaviour, as the systems never seem to converge near the same value of dissipation constant. This gives rise to the need of further investigating these systems and why it's important to consider their fundamental aspects.

Initially, if the simulation is not forced after starting, the energy in the system quickly decays away and any turbulence that is present dies off through the energy cascade. We avoid this through adding forcing terms directly to the equations the simulation solves, which constantly inject energy back into the turbulent system. Isotropic turbulence can be viewed as turbulence in a fluid flow that is largely distant from any boundaries. This could be visualized as a sample volume of water in a deep ocean where there are no objects present that might agitate the fluid in a certain way.

To alter the MHD equations, we add the terms into the equations 2.45 and 2.46:

$$\partial_t \boldsymbol{U} = -\boldsymbol{U}(\boldsymbol{U} \cdot \nabla) - \frac{1}{\rho}\nabla p + \nu(\nabla^2 \boldsymbol{U}) + \frac{1}{\rho}(\nabla \times \boldsymbol{B}) \times \boldsymbol{B} + \boldsymbol{F}_k \tag{2.97}$$

$$\partial_t \boldsymbol{B} = (\boldsymbol{B} \cdot \nabla)\boldsymbol{U} - (\boldsymbol{U} \cdot \nabla)\boldsymbol{B} + \eta\nabla^2 \boldsymbol{B} + \boldsymbol{F}_B \tag{2.98}$$

Our code has the ability to investigate both kinetic and magnetic homogeneous forcing, and certain methods of kinetic forcing have been investigated previously [9], [4]. In this report, we also look briefly at forcing the system both kinetically and magnetically. This gives interesting results that deal with certain complex self-organized flow structures, which are analyzed in the results section 4.2.

2.3.6 Fourier Transform of the MHD Equations

To finalize this chapter's section on MHD, we use the same process presented in 2.1.2 to derive the Fourier transform of the MHD equations. These equations are used explicitly in the spectral portions of the simulation program to solve for certain field fluctuation values. We first define the magnetic field's Fourier transform:

$$B_\alpha(\boldsymbol{k}, t) = \left(\frac{1}{2\pi}\right)^3 \int d^3x B_\alpha(\boldsymbol{x}, t) e^{-i\mathbf{k}\cdot\mathbf{x}} \tag{2.99}$$

and the velocity field's FT was defined by 2.11.

Taking the Fourier transform of the forced MHD equation of motion (2.97) and the and induction equation (2.98) involves the same linear transform operation on both equations, as seen in section 2.1.2. We begin by taking the fourier transform of the fourced MHD equation of motion with the gauge $p = p' + \frac{1}{2}\boldsymbol{U}^2$, so that 2.97 is altered in terms of vorticity, $\boldsymbol{\omega} = \nabla \times \boldsymbol{U}$:

$$(\partial_t + \nu k^2)\, \boldsymbol{U}(\boldsymbol{k},t) = \mathcal{F}\Big[\frac{1}{\rho}\boldsymbol{j}(\boldsymbol{x},t) \times \boldsymbol{B}(\boldsymbol{x},t)\Big] + \\ \mathcal{F}\Big[\boldsymbol{U}(\boldsymbol{x},t) \times \boldsymbol{\omega}\Big] + \boldsymbol{F}_k(\boldsymbol{k},t) - \frac{i\boldsymbol{k}}{\rho} p(\boldsymbol{k},t) \quad (2.100)$$

And the Fourier transform of the forced induction equation 2.98, noting that $(\boldsymbol{B}\cdot\nabla)\boldsymbol{U} - (\boldsymbol{U}\cdot\nabla)\boldsymbol{B} = \nabla \times (\boldsymbol{U} \times \boldsymbol{B})$, gives:

$$\partial_t \boldsymbol{B}(\boldsymbol{k},t) = \mathcal{F}[\nabla \times (\boldsymbol{U}(\boldsymbol{x},t) \times \boldsymbol{B}(\boldsymbol{x},t))] - \eta k^2 \boldsymbol{B}(\boldsymbol{k},t) + \boldsymbol{F}_B(\boldsymbol{k},t) \quad (2.101)$$

We then express the non-linear terms in the above equations as convolutions, similar to the process seen earlier (2.16). For eqn. 2.100 this gives:

$$(\partial_t + \nu k^2)\, \boldsymbol{U}(\boldsymbol{k},t) = \frac{1}{\rho} \int d^3q [\boldsymbol{U}(\boldsymbol{q}) \times \boldsymbol{\omega}(\boldsymbol{k} - \mathbf{q}, t)] \\ + \int d^3q [\boldsymbol{j}(\boldsymbol{q},t) \times \boldsymbol{B}(\boldsymbol{k} - \boldsymbol{q}, t)] + \boldsymbol{F}_k(\boldsymbol{k},t) - \frac{i\boldsymbol{k}}{\rho} p(\boldsymbol{k},t) \quad (2.102)$$

or

$$\begin{aligned} (\partial_t + \nu k^2)\, \boldsymbol{U}(\boldsymbol{k},t) &= \boldsymbol{\Pi}(\boldsymbol{k},t) + \boldsymbol{F}_k(\boldsymbol{k},t) - \frac{i\boldsymbol{k}}{\rho} p(\boldsymbol{k},t) \\ (\partial_t + \nu k^2)\, U_\alpha &= P_{\alpha\mu}\Pi_\mu + (F_k)_\alpha \end{aligned} \quad (2.103)$$

Where $P_{\alpha\mu}$ is the projection operator, defined in 2.20, which enforces the solenoidal portion of the velocity field and removes any added divergent behaviour. The steps involved in getting to the last line was the process performed in eqns. 2.18 through 2.19.

The same process is followed through convolution of the non-linear term in the induction equation (2.101):

$$\begin{aligned} \partial_t \boldsymbol{B}(\boldsymbol{k},t) &= \int d^3 j [\boldsymbol{k} \times (\boldsymbol{U}(\boldsymbol{j},t) \times \boldsymbol{B}(\boldsymbol{k} - \boldsymbol{j}, t))] - \eta k^2 \boldsymbol{B}(\boldsymbol{k},t) + \boldsymbol{F}_B(\boldsymbol{k},t) \\ \partial_t \boldsymbol{B}(\boldsymbol{k},t) &= \boldsymbol{X}(\boldsymbol{k},t) - \eta k^2 \boldsymbol{B}(\boldsymbol{k},t) + \boldsymbol{F}_B(\boldsymbol{k},t) \end{aligned} \quad (2.104)$$

Equations 2.103 and 2.104 give the appropriate transforms of the forced MHD equations we utilize in our simulations. We also define, for the sake of completeness, the magnetic energy spectra, derived with the process shown in section 2.2.2:

$$E_B(\boldsymbol{k},t) = \frac{k^2}{2} \int_\Omega d\Omega \langle |\boldsymbol{B}(\boldsymbol{k},t)|^2 \rangle \quad (2.105)$$

2.4 Self-Organization in MHD

Self-organization can be understood as large coherent structures being formed from small scale non-linear interactions independently of initial conditions. These behaviours have been investigated with homogeneous istropic forced simulations in both HD [24] and MHD [15]. States of such nature are said to be *self-organized* or *relaxed*, and the only parameters they appear to depend on are external, e.g. boundary conditions or an applied current. This topic is of interest because of the non-linear nature of turbulence itself, where despite what the conditions are at the start of the system's time state, coherence can suddenly be re-obtained. There are have been speculations that this could be one reason the universe, though heading towards a state of higher entropy, has a tendency through nonlinear energy dissipation to self-organize critically [25]. Simulating these flows has been investigated in many different ways, such as forcing through the usage of a toroidal external magnetic field [26] [27].

It should also be noted that as the magnetic and cross helicities rely on the alignment of the fields, a self-organized state then should show a maximal relative helicity (either cross or magnetic, depending on the type of alignment) value over time of +1/-1. For an extended outlook and deeper insight into self-organizing flows, see [4] and [28]. In this section we present some of the basic theory behind these states and how the alignments/anti-alignments of different fields affect the MHD equations.

2.4.1 Beltrami and Alfvénic Fields

When an MHD system is in a laminar state (that is, equilibrative or non-turbulent), it is defined as being 'force free,' and the Lorentz force term found in 2.45 is zero:

$$(\nabla \times \boldsymbol{B}) \times \boldsymbol{B} = \boldsymbol{j} \times \boldsymbol{B} = 0 \tag{2.106}$$

the pressure is unchanging or constant ($\nabla p = 0$) and $\boldsymbol{j}$ is parallel to $\boldsymbol{B}$. This gives:

$$\boldsymbol{j} = \alpha(\boldsymbol{x})\boldsymbol{B} \tag{2.107}$$

or

$$\nabla \times \boldsymbol{B} = \frac{\alpha}{\mu_0}\boldsymbol{B} \tag{2.108}$$

This state is called a Beltrami state, where $\boldsymbol{B}$ is parallel to the current. These states have been seen in hydrodynamics (although we consider on $\boldsymbol{U}$, where $\nabla \times \boldsymbol{U} \sim \boldsymbol{U}$) as well [24], and characteristically at a full state of self-organization, there is no transfer of energy between differing wavenumbers in spectral space (e.g. the transfer spectra should be zero at all wavenumbers). If we take the divergence and curl 2.108 we derive two equations that allow us to solve for α and $\boldsymbol{B}$:

$$\boldsymbol{B} \cdot \nabla \alpha = 0 \tag{2.109}$$

$$\nabla^2 \boldsymbol{B} - \left(\frac{\alpha}{\mu_0}\right)^2 \boldsymbol{B} = \frac{1}{\mu_0}(\nabla \alpha \times \boldsymbol{B}) \tag{2.110}$$

Where the top equation shows that $\alpha(\boldsymbol{x})$ is a constant when following a magnetic field line. Notice that when our system exhibits a Beltrami flow, then $\boldsymbol{j} \times \boldsymbol{B} = 0$, and the projection term of $\boldsymbol{A}$ and $\boldsymbol{B}$ in magnetic helicity (2.82) maximizes.

With the instance of Beltrami flows, there is the possibility of a second self-organizing state occurring independently or alongside: Alfvénic states. This is where the magnetic and velocity fields align with one another ($\boldsymbol{B} \propto \pm \boldsymbol{U}$) and the first term in 2.46 disappears:

$$\boldsymbol{U} \times \boldsymbol{B} = 0 \tag{2.111}$$

This produces a system with a cross helicity that dominates (2.90) where the projection between $\boldsymbol{U}$ and $\boldsymbol{B}$ is maximized (when normalized, $H_C \rightarrow +1$) or minimized (-1). It is possible to see either self-organizing behaviours occur independently or at the same time. This is seen as a 'flat-lining' of total system energy over time where the cross/magnetic helicities over time approach +1/-1, depending on their initial alignment, and comes with no preference of initial conditions (non-linearity) [15]. It's been observed in nature that solar-wind magnetohydrodynamic turbulence is observed to be mainly made of Alfénic fluctuations that propagate away from the sun. This was shown to be due to the an asymmetry seen between modes with high amounts of cross helicity (+1/-1) [29].

2.4.2 The Inverse Cascade

As discussed before, in neutral fluid flows there is the presence of the energy cascade, where at large configuration space scales the energy flows down to the level of dissipation at very small scales. In 1973, however, it was seen in MHD flows that there were certain buildups of magnetic energy density at small wavenumbers that were larger than the kinetic energy density [30].

This led to the possibility of a magnetic energy inverse cascade, where magnetic energy traveled opposite the direction of the kinetic energy and built magnetic fields at larger scales than what was evident from observed fluid motion. It was later investigated through DNS in 3-D MHD by [31] and was shown to be a mostly a direct effect of magnetic helicity moving away from large forced wavenumbers to small ones.

There have also been physical observations of the inverse cascade in systems such as wall bounded sheer flows or rotational flows [32], but there is still little known of it when it comes to homogeneous isotropic turbulence. [31] also mentions that though magnetic helicity plays a large contribution to the inverse cascade, it is not necessary for the generation of large scale magnetic fields as there exists a dynamo action, discussed in the next subsection.

2.4.3 The Dynamo Effect

We briefly mention the *dynamo effect*, as the mechanic of kinetic to magnetic energy transfer is important in MHD. It is commonly known that the kinetic movements of charge induces a magnetic field, or as an ensemble average contributes to an overall magnetic field. This effect is called the dynamo effect (DE), and is commonly seen in MHD. The dynamo effect has been observed in nature as well, contributing towards the complex nature of the sun's external magnetic field [22] and speculated to be the cause of the geomagnetic field by the mantle of the earth's crust moving and liquid turbulent metal in its core [33].

We should expect to see the DE in our simulations, as we kinetically force in all simulations. This will be indicated through a finite magnetic energy over time, even if no magnetic energy is explicitly injected. The system becomes energetically balanced from an exchange between the Lorentz force term in eqn. 2.45 and the dynamo effect.

Chapter 3

Method and Direct Numerical Simuations

The manner in which a computational fluid dynamics (CFD) simulation is created can vary greatly. Choosing a specific method comes with the need to balance accuracy/resolution with system complexity (e.g. large topological distortions) and computational efficiency. What makes numerical simulations so advantageous is they allow control over most parameters and initial conditions can be reproduced very easily. Anything from accurately reproducing experimental results to simulating a system that would be difficult to create experimentally (such as homogeneous isotropic turbulence) is what has made numerical simulations so popular.

One calculation method in particular, Direct Numerical Simulations (DNS), iterates through all large (small k) scales in configuration space to turbulence at the smallest scales needing to be considered (such as the Kolmogorov microscale, eqn. 2.28). Other simulation methods, such as Large Eddy Simulations (LES), can be more efficient than DNS, but lack the ability to emulate a real flow to a level of accuracy DNS is able to obtain. This is because LES only considers the larger scales of turbulence and statistically 'guesses' at what happens in smaller scales of configuration space [34]. In other words, LES methods tend to be less demanding when it comes to computational time, but sacrifice accuracy as a result. In contrast, since DNS considers all scales, it is much more accurate, but requires a larger amount of computational power.

3.1 Pseudospectral DNS

For a hydrodynamic turbulence simulation, the basic algorithmic structure is that a computer solves the Navier-Stokes equation (2.8) for $\boldsymbol{U}(\boldsymbol{x},\, t)$ at time t, then the vorticity $\boldsymbol{\omega} = \nabla \times \boldsymbol{U}$, makes a differential time step and reiterates at $t + \delta t$, and continues to do so until it is told to stop at a specific simulation time. Transitioning into MHD requires additional components so that the intrinsic magnetic field interactions are accounted for. As these simulations are quite complicated and DNS evaluates at every scale, utilizing a spectral technique can help reduce some of the computation time. For this report, we use a pseudospectral DNS method, which involves Fourier transforming back and forth between Fourier space and configuration space to solve selective portions of the MHD equations. Pseudospectral takes advantage of the faster compute times involved in spectral space, where all the linear divergence terms in configuration space transform into multiplicative operations (as seen in sections 2.1.2, 2.3.6).

Spectral techniques are not the only method DNS can use, as there exists grid methods such as Finite Difference (FDM) and Finite Volume methods (FVM) [35]. These use local information to estimate derivatives in different points of the system's grid or within specific volume integrals. FDMs utilize difference operators to approximate derivatives, and FVMs convert derivatives in volume integrals to surface integrals, only considering the flux. We mention these purely for the sake of example, and choose solely to use spectral DNS for our results. Spectral DNS differs in that it is an expansion of the solutions to our MHD equations in terms of a set of orthogonal basis polynomials.

The pseudospectral DNS code used for all of our simulations was originally written by Sam Yoffe [3], and its MHD adaptation was crafted by Moritz Linkmann [4]. It was written through the Message Passing Interface (MPI) library utilizing Fast Fourier Transforms (FFT) from the FFT library to switch between configuration and Fourier space to efficiently compute different operations present in the Navier-Stokes MHD equations. The algorithm performed in N^3 space for the pseudospectral process is as follows [8]:

1. Each point is assigned three Gaussian random numbers and initially generates a $t = 0$ velocity and magnetic field: $\boldsymbol{U}(\boldsymbol{x},\, 0)$, $\boldsymbol{B}(\boldsymbol{x},\, 0)$. These random Gaussian numbers are given a mean of 1 and variance of 0 [3] (see 3.2.1 for more details).

2. Use FFT to move to Fourier space, solving the forced MHD equations (2.97, 2.98) for general t: $\boldsymbol{U}(\boldsymbol{k},\, \mathrm{t})$, $\boldsymbol{B}(\boldsymbol{k},\, \mathrm{t})$. With these values, voriticity $\boldsymbol{\omega}(\boldsymbol{k}, t)$ (in Fourier space: $\boldsymbol{\omega} = i\boldsymbol{k} \times \boldsymbol{U}$), current $\boldsymbol{j}$ ($\boldsymbol{j} = i\boldsymbol{k} \times \boldsymbol{B}$), and the non-linear term in the FT induction equation (2.104): $i\boldsymbol{k} \times (\boldsymbol{U} \times \boldsymbol{B})$ are solved.

3. FFT backwards to configuration ($\boldsymbol{x}$) space to find all non-linear terms in both of our MHD equations (2.45 & 2.46).

4. FFT back to Fourier space to find the first term in 2.103, then taking the operation defined in the second step of 2.103 with the projection operator, $P_{\alpha\mu}$. As specified in section 2.1.2, this operation ensures the solenoidal nature of our fields and cancels all mean-flow components.

5. Force the system at a set forcing strength and type.

6. Move forward a single set differential time step, δt, by solving the MHD equation of motion (2.45) and the induction equation (2.46) for $\boldsymbol{U}(\boldsymbol{x}, \delta t + t)$ and $\boldsymbol{B}(\boldsymbol{x}, \delta t + t)$

7. If the time step doesn't exceed the set simulation time limit, repeat the process until so.

This process is a single iteration of the code and a single simulation can move through several thousand time steps. When simulating larger systems, such as 512^3, a simulation time step is set at $dt = 0.0006$, so that the system is fully evaluated around every

$\sim 1/1600^{th}$ of a second in simulation time. This is why utilizing MPI becomes necessary, as at each site ($512^3 \sim 1.3 \times 10^8$) an entire loop of what is described above has to occur at several different configuration scales.

In the next section we describe some of the resolution problems that can occur with the usage of multiple Fast Fourier Transforms and how they are accounted for. The usage of MPI creates the problem of separating processes between different processors, where no memory is stored - but the simulation itself must be interactive (e.g. there must be non-local knowledge at each site). The code we use overcomes this problem and certain aliasing errors do not appear in the final outputs.

3.2 Computing Techniques

3.2.1 Initial Fields and Anti-aliasing

When simulating a turbulent system, in concern to computational efficiency, it is often important to start the simulation at a point where a fluid would *assumingly* already be turbulent. If this were not the case, then it would take a large amount of time to get the system to a point where we could start considering the solutions to the MHD equations. This problem is addressed through the generation of a Gaussian field for both initial quantities ($\boldsymbol{U}$ & $\boldsymbol{B}$). As described in the steps above, in the initial system when the projection operator ($P_{\alpha\mu}$) is applied and our field remains solenoidal, the energy spectra (2.37) is determined and each mode in Fourier space is then rescaled by [3]:

$$U_\alpha(\boldsymbol{k}, 0) \rightarrow U_\alpha(\boldsymbol{k}, 0) \cdot \sqrt{\frac{E(k,0)}{E(k,t)}} \tag{3.1}$$

which produces a usable energy spectrum, allowing us to skip the process of arriving at a turbulent state from an initially motionless flow. In accordance to the original author of the code [3], truncation is used to address the aliasing errors that occur. Aliasing arises when the code does several FFTs in succession, and is caused by faulty Fourier mode coupling.

3.2.2 Checking and Running the Code

It is always important, when creating or using a pre-written simulation software, to check against prior results to ensure whether or not the code is operating correctly. This was done by comparing initial simulations against those presented in in D. Clark's [9] report and results obtained by [4], as their work closely reflected what we have done and they both used the similar versions of the software.

For all simulations performed and results presented, the UK's national computing service Archer (http://www.archer.ac.uk/) was used for large system size simulations (256^3) and the University of Edinburgh's Linux Cluster: Eddie for 128^3 runs. Several comparison simulations were run with identical input values on both supercomputers to ensure we received identical results and the software packages on each were performing correctly. These results were for different forcing methods with 128^3 systems, and gave the same output. Larger runs at 512^3 were attempted, but were difficult to test in timely fashions due to the queue times on Archer (around 7 days per $\sim 15s$ simulation time).

To begin the simulations an input script was edited and submitted via a bash or .pbs script. The input files contained all useful system parameters we wished to simulate, such as viscosity or forcing type, and a seed value was chosen. As stated beforehand, for every simulation we choose a Prandtl value of one (so that kinetic effects are not dominant over magnetic effects of vice-versa) and both initial cross and magnetic helicities are set to zero. Input values for simulations that were successful and used in the final results are given in appendix A.1.

Energy Spectra Hooks

As it will be shown, certain 'hook' like shapes will arise in our energy spectra at the largest wavenumber cutoff in our simulations. Due to the nature of DNS, this is because of a pile-up of energy that occurs in the simulation after the cutoff point (i.e. the Kolmogorov scale) and hasn't dissipated out because the simulation only goes to k_{max}. We neglect this portion of the curves, and only consider the behaviour of the energy spectra before these hooks appear.

3.3 Forcing Functions for Isotropic Turbulence

The non-linear dissipation terms seen in the MHD equations (2.97 & 2.98) leads to energy dissipation that falls from large to small scales in configuration space. This process must be countered through adding a forcing term, which was introduced in section 2.3.5. These forcing terms must be divergenceless, and homogeneous/isotropic. This non-linear nature of turbulence also leads to the concept that a system which is homogeneously turbulent should in fact independently arrive at such a state no matter the manner in which it was forced there to begin with. In other words, one should arrive at similar results independently of the initial conditions. This has been shown to be correct in HD and partially in MHD [9], and we further extend the results that were presented in these reports by investigating in more depth a third method of forcing.

We use three different methods to derive our results at different system sizes:

1. Negative Damping (ND)
2. Adjustable Helicity (AHF)
3. SinForce (SF)

In this section we present the background theory behind these forcing methods and specify what system sizes were used for each manner of forcing (kinetic or magnetic). Note that though [8] investigated magnetic forcing in MHD, it was at very small system sizes (32^3) with sinforcing and the runs were for the sake of implementing the forcing type into the code. This method has already been investigated magnetically by [15], so we choose to investigate only ND and AHF magnetic/kinetic methods. While [9] investigated larger systems (up to 512^3) for sinForcing, there were only a small number of total runs completed. We extend upon his kinetic forcing results, and further address some of the conserved quantity issues seen in his report.

For all defined methods below, there are specific ranges in wavenumbers that the forcing operators extend to (the maximum forced k value being k_f). Our results, as this report is focused on large scale forcing, only force to either $k_f = 2$ or $k_f = 3$. The value will be specified when appropriate.

3.3.1 Negative Damping

The first forcing method, negative damping, was developed by L. Machiels [36], who by observing the occurrence of self-organized structures in turbulence, sought to develop a method that balanced this self-organizing probability (or coherence) with the randomized non-linearity associated with turbulence. To begin, we design two dissipation constants, ϵ_1 and ϵ_2, to effectively balance energy transfer. This is crafted from the total energy leaving the system:

$$E_{out} = \epsilon_k + \epsilon_B = \epsilon_{tot} \tag{3.2}$$

where ϵ_k is the kinetic dissipation and ϵ_B the magnetic dissipation. These two terms summed together lead to the total dissipation, ϵ_{tot}. At a steady state, we require energy leaving = energy coming in. This is done by:

$$E_{out} = \epsilon_k + \epsilon_B = E_{in} = U_\alpha(F_k)_\alpha + B_\alpha(F_B)_\alpha \tag{3.3}$$

Where $(F_k)_\alpha$ and $(F_B)_\alpha$ are the kinetic and magnetic forcing terms. For negative damping these are defined by:

$$(F_k)_\alpha(\boldsymbol{k}, t) = \begin{cases} \epsilon_1 U_\alpha(\boldsymbol{k}, t)/[2E_{k,f}(t)], & if\ 0 < k \leqslant k_f \\ 0, & else \end{cases}$$

Where ϵ_1 is an arbitrary dissipation constant and $E_f = \int_0^{k_f} E(k,t)dk$. $E(k,t)$ is the energy spectrum at simulation time, t, and k the given wavelength. Essentially, the forcing function feeds the velocity field back into itself. Likewise we define the magnetic forcing function (which feeds the magnetic field back into itself):

$$(F_B)_\alpha(\boldsymbol{k}, t) = \begin{cases} \epsilon_2 B_\alpha(\boldsymbol{k}, t)/[2E_{B,f}(t)], & if\ 0 < k \leqslant k_f \\ 0, & else \end{cases}$$

Where ϵ_2 is a second arbitrary dissipation constant defined above and $E_{B,f} = \int_0^{k_f} E_B(k,t)dk$ the magnetic energy spectrum integrated over all considered wavenumbers $k \in [0, k_f]$

where k_f is the largest forced wavenumber. This then leads allows us to choose the two dissipation constants to equal in summation the total dissipation:

$$\epsilon_1 = \epsilon_2 = \frac{1}{2}\epsilon_{tot} \tag{3.4}$$

Due to the nature of negative damping, magnetic/cross helicity have the possibility of getting 'stuck' in certain value wells (as ND never changes the alignment of the fields), and there is no way directly to alter any injected helicities. This implies if they approach maximized values over time (never fluctuating, but randomly can select either +1 or -1) due to the field's unaltered alignment with each other, they will only grow. We investigate this further in our results section.

3.3.2 Adjustable Helicity

The second form of forcing we investigate is called adjustable helicity, this method was used with DNS in HD by [37] and for MHD by [4]. Instead of feeding the fields back into the system as ND does, it allows control over the injection of magnetic helicity. The forcing function for AHF is given by:

$$\boldsymbol{F}(\boldsymbol{k}, t) = A(\boldsymbol{k}, t)\boldsymbol{e}_1(\boldsymbol{k}) + B(\boldsymbol{k}, t)\boldsymbol{e}_2(\boldsymbol{k}) \tag{3.5}$$

where $A(\boldsymbol{k}, t), B(\boldsymbol{k}, t) \in \mathbb{C}$ are the complex coefficients defined as:

$$\begin{aligned} A(\boldsymbol{k}, t) &= [f(k)]^{\frac{1}{2}} g_A e^{i\alpha(\mathbf{k})} \\ B(\boldsymbol{k}, t) &= [f(k)]^{\frac{1}{2}} g_B e^{i\alpha(\boldsymbol{k})} \end{aligned} \tag{3.6}$$

For normalization factors $f(k)$, the two unknowns g_A, g_B satisfy $g_A^2 + g_B^2 = 1$, and a random local Gaussian phase factor for each term: $e^{i\alpha(\boldsymbol{k})}$ which is re-inserted for each segment of time in the simulation (dt). These terms (3.6) are the fundamental constructs behind the AHF method that determine an altered relative helicity injected into the system. We define this relative helicity as:

$$\rho_f = \frac{H_f}{k|\boldsymbol{F}(\boldsymbol{k}, t)|^2} \tag{3.7}$$

and also define $\boldsymbol{e}_1$ and $\boldsymbol{e}_2$ with the conditions:

$$\boldsymbol{e}_1 \cdot \boldsymbol{e}^{\boldsymbol{*}}{}_2 = 0 \tag{3.8}$$

and because the fields are divergenceless:

$$\boldsymbol{e}_1 \cdot \boldsymbol{k} = \boldsymbol{e}_2 \cdot \boldsymbol{k} = 0 \tag{3.9}$$

to be the eigenfunctions of the curl operator [37]:

$$\boldsymbol{e}_i = \frac{\boldsymbol{k} \times (\boldsymbol{k} \times \hat{\boldsymbol{e}}_j) - i|\boldsymbol{k}|(\boldsymbol{k} \times \hat{\boldsymbol{e}}_j)}{2k^2\sqrt{1 - (\boldsymbol{k} \cdot \hat{\boldsymbol{e}}_j)^2/\mathbf{k}^2}}, \quad i = 1,2 \quad j = 1,2,3 \tag{3.10}$$

where $\hat{\boldsymbol{e}}_j$ is an arbitrary unit vector chosen randomly that creates through its cross product with $\boldsymbol{k}$ a non-parallel vector to $\boldsymbol{k}$:

$$i\boldsymbol{k} \times \boldsymbol{e}_1(\boldsymbol{k}) = k\boldsymbol{e}_1(\boldsymbol{k}), \quad i\boldsymbol{k} \times \boldsymbol{e}_2(\boldsymbol{k}) = -k\boldsymbol{e}_2(\boldsymbol{k}) \tag{3.11}$$

Which allows us to re-define the forced relative helicity as [4]:

$$\rho_f = \frac{H_f(k)}{k|\boldsymbol{F}(\boldsymbol{k},t)|^2} = \frac{g_A^2 - g_B^2}{g_A^2 + g_B^2} = g_A^2 - g_B^2 \tag{3.12}$$

To alter this injected relative helicity - we choose a fixed angle ϕ and set $g_A = cos(\phi), g_B = sin(\phi)$. As stated prior, we investigate in our results the magnetic and kinetic forcing methods with AHF. Using AHF, magnetic and/or kinetic helicity energy then would be injected into the system (the normalized values of 2.82 and 2.81 respectively).

3.3.3 Sinforce

The final method of forcing, sinforce, utilizes a sinusoidal method of randomized periodic/deterministic fluctuations, and is non-helical. This was developed by [15] where they investigated self-organizing behaviours at large system times in MHD (but enforced a randomizing element, which also produced some non-self-ordering states). This method was implemented into our code by [8] who only slightly investigated the effects of magnetic forcing at small system sizes. Kinetic sinforcing is defined as:

$$\boldsymbol{F}_f = f_0 \sum_{k>0}^{k_f} \begin{pmatrix} sin(kz) + sin(ky) \\ sin(kx) + sin(kz) \\ sin(ky) + sin(kx) \end{pmatrix} \tag{3.13}$$

Where f_0 is a set kinetic constant, and similar to prior methods we force in the range of $0 \; to \; k_f$. We also define a magnetic forcing for SF:

$$\boldsymbol{F}_B = g_0 \sum_{k>0}^{k_f} \begin{pmatrix} -sin(kz) + sin(ky) \\ -sin(kx) + sin(kz) \\ -sin(ky) + sin(kx) \end{pmatrix} \tag{3.14}$$

Likewise, g_0 is a set magnetic constant, and for all results obtained we force the same range kinetically as we do magnetically, so k_f will always be identical between the two.

Summary

This concludes our method section, where began with the discussion of the software algorithm used to obtain our results. Then, we briefly touched on the techniques used to build initial system values and the computing facilities used to simulate the system. Finally, we presented the structure of the forcing functions and how they tie in MHD theory. The next chapter gives the results we have derived from the described code in this chapter, understood through the theory given in chapter 2.

Chapter 4

Results

In this section we present the results from our simulations in a split structure. First, we investigate systems forced solely through kinetic forcing (through the addition of a forcing term in the MHD equation for the velocity field.) To begin our investigation of the different forcing methods, energy vs. time plots are shown with comparisons of low to high Reynolds numbers (i.e. different system sizes). These plots help confirm when the turbulent flow has reached a steady state, and we observe the behaviours between different methods of forcing. Then we compare the relative magnetic and cross helicities of different Reynolds numbers, addressing certain issues with these ideal invariants presented by [9] through looking at extended simulation times. From the results found in the prior two subsections, we point out certain points of interest in the energy and helicity structures, discussing any possible connections that could later be verified through specific simulations. The end portion of our kinetic forcing section then shows the magnetic spectra each forcing method produces at different Reynolds numbers. In this we hope to find an agreement with the power laws described in section 2.2.1. It is also important to see if the energy spectra behave similarly between ND, AHF and SF; if they do, it would confirm our speculation that the end state behaviours be independent of the initial method of isotropic/homogeneous forcing. Finally, we present the different behaviours of our transfer spectra, and expect to see energy transfer that agree with the allotted forcing techniques.

In the second and final chapter of this section, we briefly show results of systems using ND and AHF through magnetic and kinetic forcing. The results in this chapter are up to much interpretation, and due to project time constraints we lightly touch of the noticeable details and behaviours of the ideal conserved quantities. What can be said is that with both methods, certain self-organized states form either partially or fully, we present flow visualizations to enforce this result.

4.1 Kinetic Forcing

In this section we observe the different quantities each system has through all three methods of kinetic forcing: ND, AHF, and SF. All runs were done with a Prandtl number of 1, and the majority of wavenumbers forced was $0 < k \leq 2$ (where some preliminary runs were done to 3). Run input parameters for every successful simulation are located in appx. A.1.

4.1.1 Energy Over Time

We begin by observing the system kinetic and magnetic energies over time, presented in figures 4.1 and 4.2. We note that in each plot, the magnetic field energy ($E_B(t)$) reaches a steady state almost immediately, as there is no direct forcing on the $\boldsymbol{B}$ field and only on the $\boldsymbol{U}$ field. The observed sustained magnetic field is due to the dynamo effect (section 2.4.3).

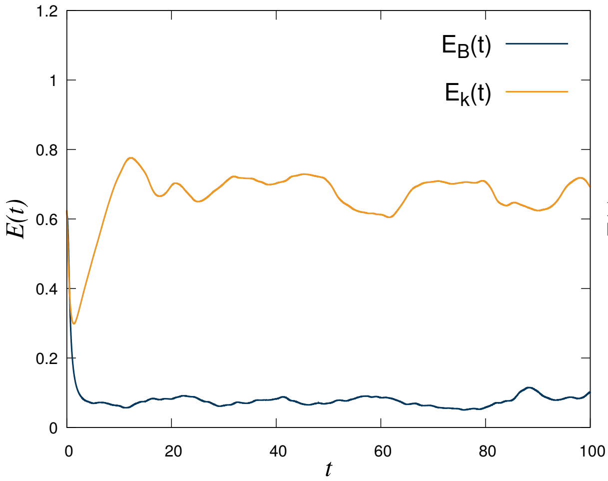

(a) ND, $Re = 101.04$.

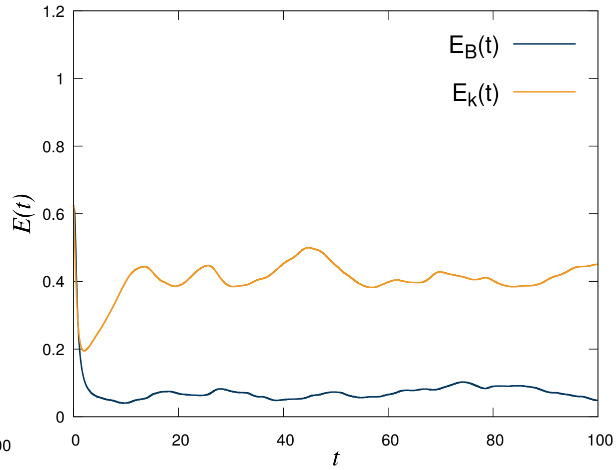

(b) AHF, $Re = 108.20$.

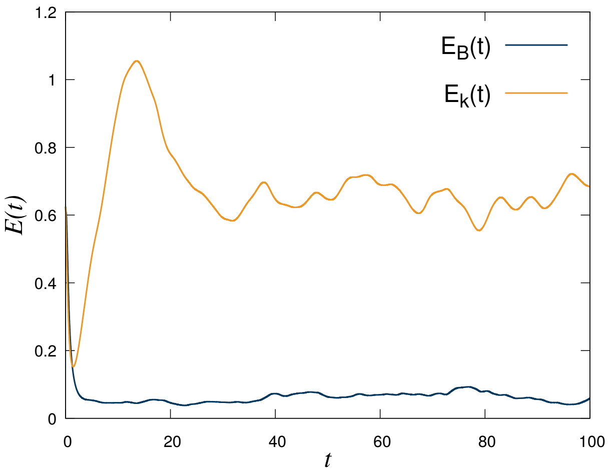

(c) SF, $Re = 112.75$.

Figure 4.1: Three figures of magnetic and kinetic energy vs. time marked with their respective forcing method and at system size 128^3. All Re values are taken as an average from $t = 20s$ to $t = 100s$. Note that the SF diagram has a slightly higher Re due to the slight contribution from the large spike of kinetic energy around $t \sim 10s$.

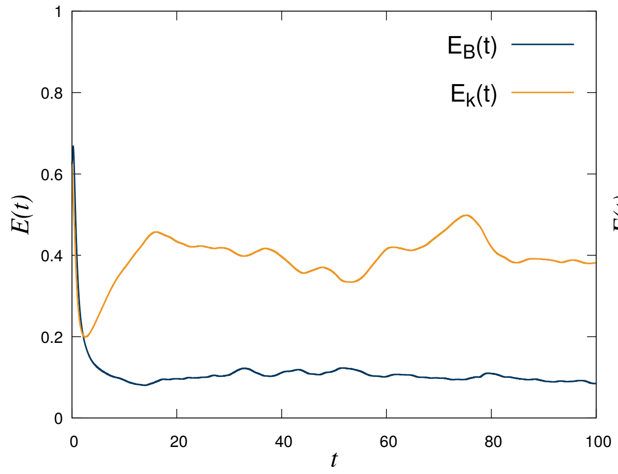

(a) ND, $Re = 342.23$.

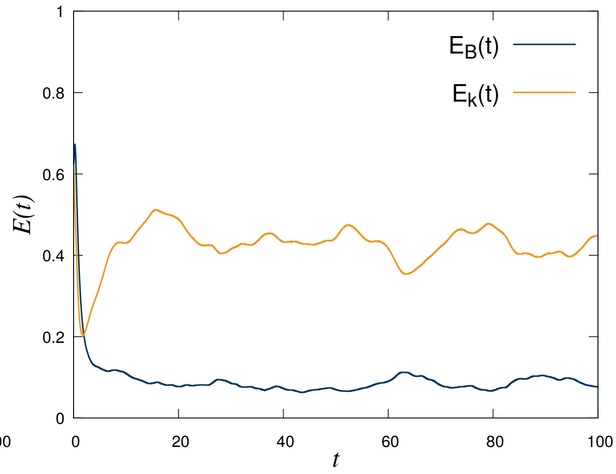

(b) AHF, $Re = 334.9$.

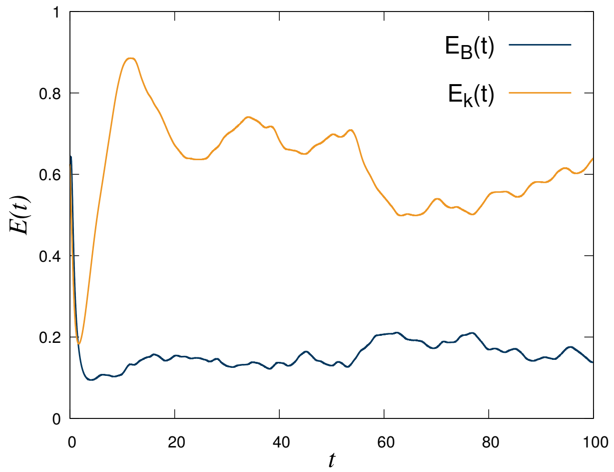

(c) SF, $Re = 357.4$.

Figure 4.2: Three figures of magnetic and kinetic energy vs. time marked with their respective forcing method at system size 256^3. All Re values are taken as an average from $t = 20s$ to $t = 100s$. We see the same SF behaviour, where a large spike of energy occurs in the beginning and dies down at $t = 20s$.

One unique characteristic taken from both plots is the large spike in energy for SF that extends from $t = 0s$ to $t \sim 20s$. We may ignore this, as the initial conditions for each forcing method must be negated from our final interpretation of the results since it has not yet reached a mean steady state. ND and AHF appear to reach a steady state sooner, as the initial peaks match in magnitude those that come later (when we consider the mean of the energy it would be balanced better including the initial peaks). The SF behaviour for 256^3 is very curious around $60s$ (fig. 4.2 (c)), where a sudden drop in kinetic energy is met with a rise in kinetic energy. This is also seen in lighter effect for the AHF, where around $65s$ a drop in kinetic is met with a rise in magnetic. This could be caused by the magnetic/cross helicity values, which are dependent upon both field's alignments with one another and their magnitudes.

These results then show we have similar systems between each forcing method, and with longer run times we could further confirm this. The SF plots also agree with what was presented in section 5.4 of E. Goldstraw's report [8], where the sinforcing method was implemented and tested in MHD against negative damping forcing. All simulations have gone into a steady state after $20s$, and later we investigate certain portions of figure 4.2's plots in section 4.1.3 by comparing alongside the behaviour of the relative helicities.

4.1.2 Helicities

We now present the relative helicities found for kinetically forced MHD systems at different Re. It is important to note that as system size grows and the Reynolds number increases, the simulation will have to take into account a larger amount of degrees of freedom, and the quantities will fluctuate in less powerful strokes (i.e. the curves will tighten/smooth out).

In their results [9] notes in section 4.2.2 that their 256^3 AHF simulation might be evident of a buildup of relative cross helicity ending at a simulation run time of $70s$. In figure 4.3 (b) we present a similar buildup found in one of our 256^3 AHF simulations at the same time ($\sim 70s$.) but later is shown to return to zero. Figure 4.3 (a) shows a comparative AHF simulation's relative helicities showing a later fluctuation that could be misinterpreted as a buildup. Our findings lead us to believe [9] viewed a fluctuation; further statistics would help confirm this.

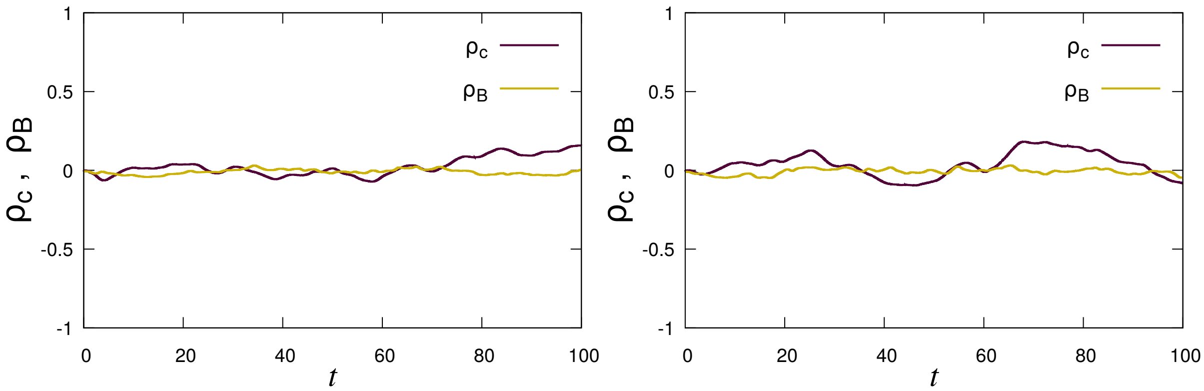

(a) AHF at 256^3, run Fb

(b) AHF at 256^3, run H1

Figure 4.3: Relative cross and magnetic helicities using AHF at system size 256^3 and $Re = 399.3$ (a). Note that in (a), there appears to be a buildup in cross helicity. However, in (b) we used the same forcing method at a similar $Re = 334.9$, leading us to believe this buildup in (a) is more likely a fluctuation.

In figure 4.4, we present the relative cross and magnetic helicity values for 128^3 and 256^3 systems. As Re increases, the relative helicities should become drawn out and stretched. SF gives the largest and longest value fluctuations for cross helicity 2.90, implying a greater alignment of $\boldsymbol{U}$ and $\boldsymbol{B}$ over the entirety of the flow (each snapshot is integrated over all space). Figure 4.4 also shows that as we increase Re, the fluctuations seen in the relative magnetic helicities for each forcing type lessen, though the usage of AHF and SF show little difference in cross helicity. Note that the alignment of $\boldsymbol{U}$ and $\boldsymbol{B}$ weakens the non-linear term in the Ind. equation, thus energy transfer maximizes when $\boldsymbol{U} \perp \boldsymbol{B}$.

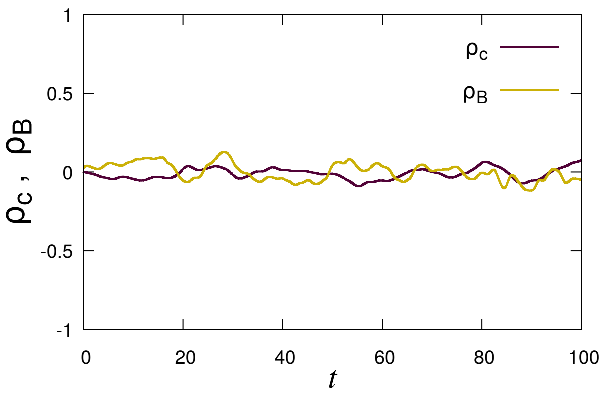

(a) ND, 128^3 and $Re = 44.5$

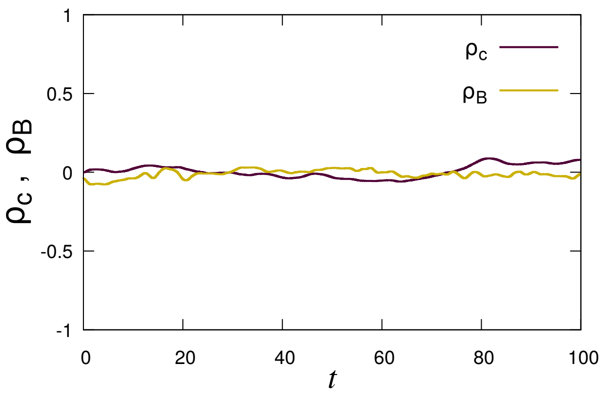

(b) ND, 256^3 and $Re = 342.2$

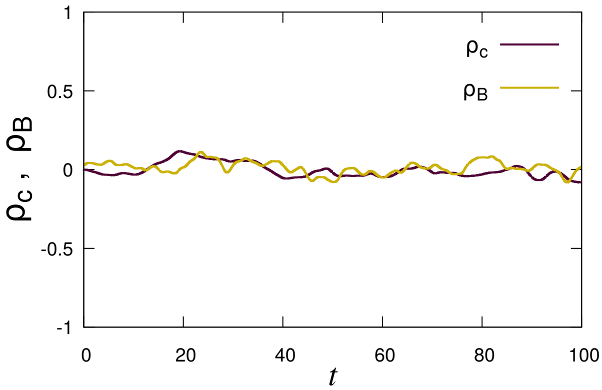

(c) AHF, 128^3 and $Re = 67.1$

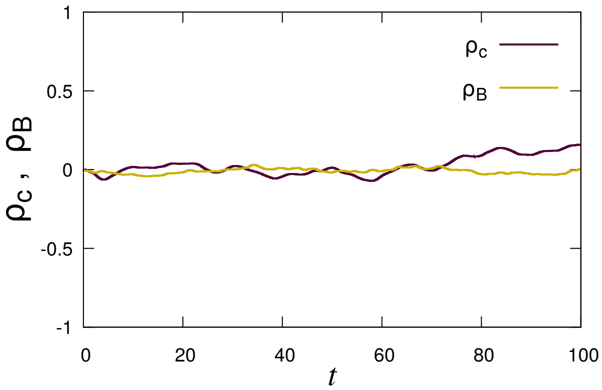

(d) AHF, 256^3 and $Re = 399.3$

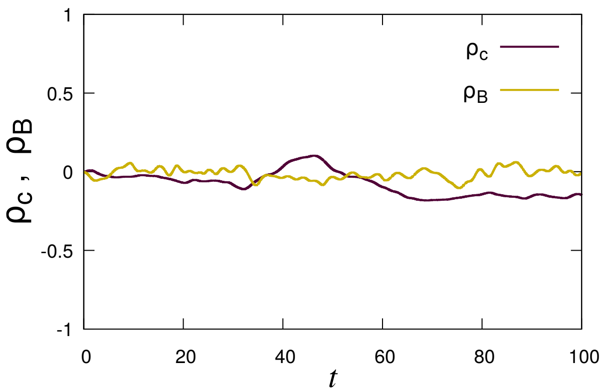

(e) SF, 128^3 and $Re = 84.0$

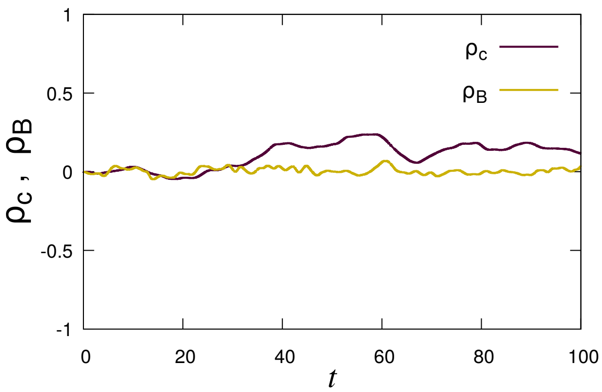

(f) SF, 256^3 and $Re = 357.4$

Figure 4.4: Relative helicities for varying system sizes/forcing types and low to high Reynolds numbers. Note that for SF in (e), (f), as we increase Re the fluctuations in the relative magnetic helicity decrease, but for cross helicity they remain relatively the same.

4.1.3 Energy and Cross Helicity Correlation

As our helicities are dependent on the alignment and strength of the MHD system's fields, we investigate any possible correlations in energy and the relative helicities (256^3 systems in figs. 4.2 and 4.4). Points of interest are given in figure 4.5, and discussed below.

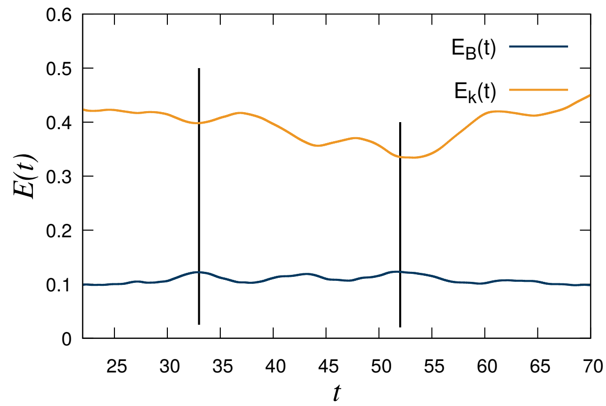

(a) ND, energy vs. time

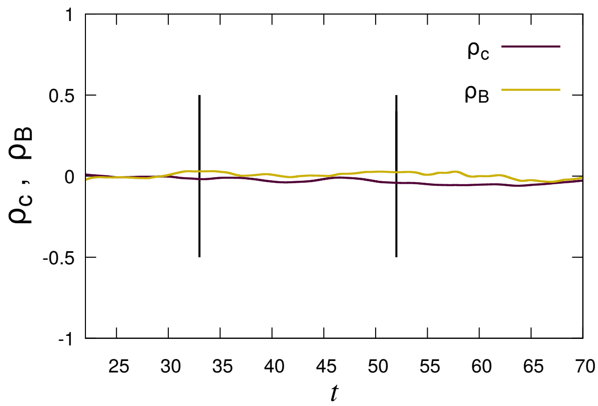

(b) ND, relative helicities

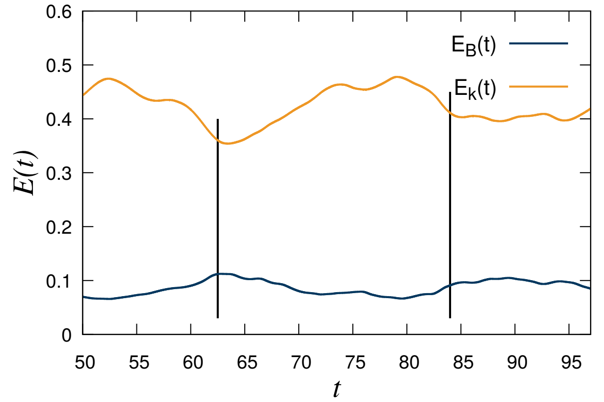

(c) AHF, energy vs. time

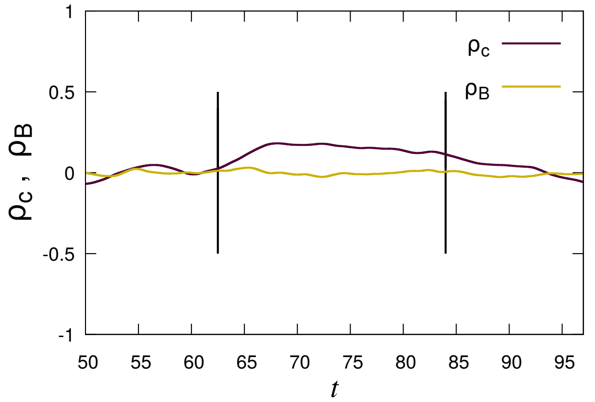

(d) AHF, relative helicities

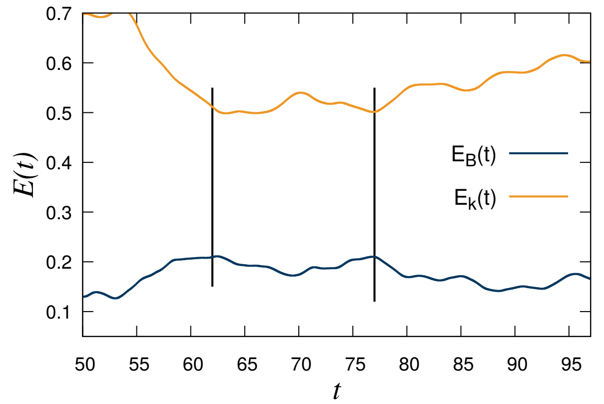

(e) SF, energy vs. time

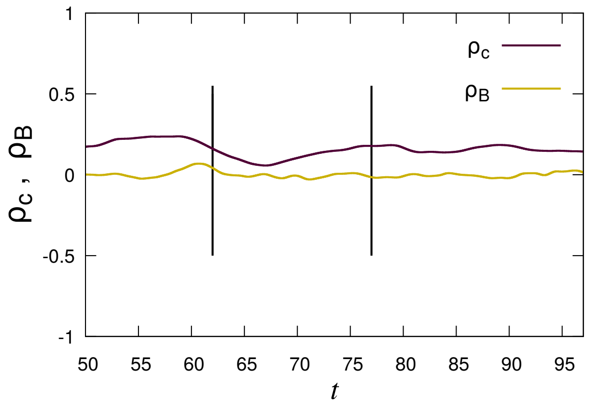

(f) SF, relative helicities

Figure 4.5: Energy vs. time plots (presented previously for 256^3 systems) with slices placed to indicate interesting energetic behaviours, e.g. where the kinetic energy drops and magnetic energy appears to rise. We seek to find a correlation between the relative helicities (right column) at these points in energy.

It should be noted that the dynamo effect contributes moreover to the sustaining of the magnetic field, implying semi-drastic features such as what is seen between the kinetic and magnetic energies in figure 4.5 (e) could more likely be attributed to the relative helicity values.

We begin our analysis with plots (a) and (b) from figure 4.5, where negative damping forcing is used. It's possible that the technique behind negative damping, where both field's values are fed back into themselves, contributes to the fact of why we see smaller and stretched fluctuations in the relative cross helicity compared to the other two methods. Though the fluctuations are small, it still behaves quite similarly to the other two methods.

Several interesting behaviours can be said about the energy and helicity correlations for the final two forcing methods: AHF and SF. The second layer of figures in 4.5, (c) and (d), show an increase of magnetic energy and decrease of kinetic energy around 62.5 seconds. An almost non-zero value of relative cross helicity increments quickly, where kinetic energy increases as well, and gradually diminishes over the course of the interval. The kinetic energy during this period appears to carry an inverse relationship with the relative CH, while the magnetic energy behaves directly.

Non-zero magnetic helicity values would deplete the Lorentz force, as $\boldsymbol{A}$ and $\boldsymbol{B}$ partially align. We see this behaviour in figure 4.5 (f), where an apparent bump in relative magnetic helicity occurs around $t = 62.5s$, followed by a leveling out of kinetic and magnetic energies. Around $65s$ there is a drop in CH, and a rise in kinetic/fall in magnetic energy. The energies appear to have an inverse relationship with one another, and the rises/falls closely correlate with the fluctuations in relative cross helicity. To the left of the center of the interval we see a local minimum in relative CH, where transfer of energy peaks, with kinetic energy increasing and magnetic energy decreasing.

Our observations of these behaviours could further be characterized through the analysis of several simulation's energy and relative helicity curves compared side by side. We have seen in this section that the behaviours of CH can indicate fluctuations in energy from curves (e) and (f), but could also be affected through the method of forcing used as well. An almost direct relationship can also be seen between magnetic energy and relative cross helicity in both pairs of figures (c),(d) and (e),(f); but more clearly with SF. This could be further clarified with higher resolution simulations.

4.1.4 Energy and Transfer Spectra

We now present the energy and transfer spectra from our 128^3 and 256^3 simulations. We expect to see in the first subsection similar behaviours between each forcing method and a characteristic power law, much like that in hydrodynamics. All results are ensemble averages, which means they were taken when the system has gone into a statistical steady state (i.e. $t \sim 20 - 100s$).

Energy Spectra

Here we present the ensemble averages of the magnetic energy spectra for all forcing methods in figure 4.6. As discussed in section 2.3.3 we plot a reference $k^{-\frac{3}{2}}$ law in for comparison. Note that these are spectra, so they are depicted in wavenumber space.

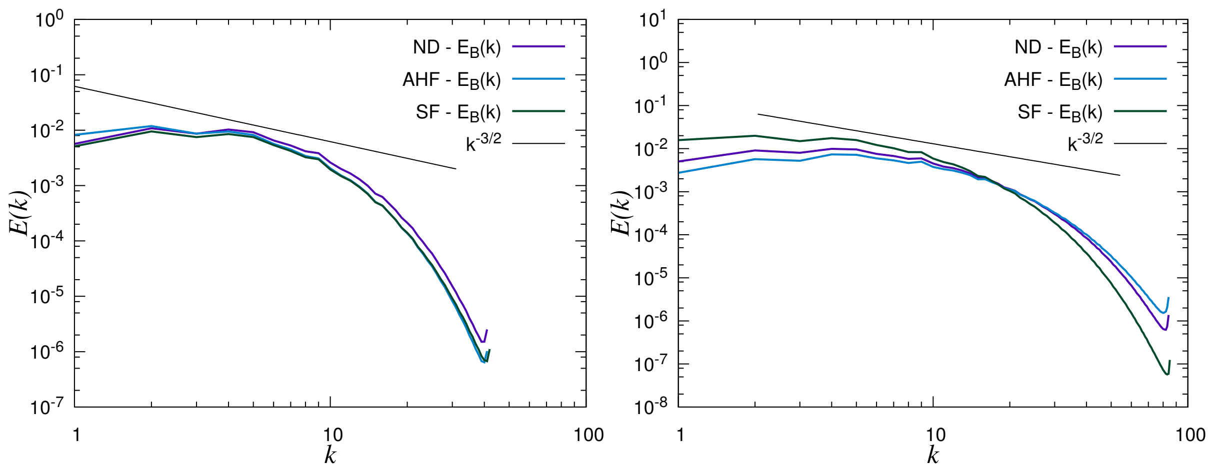

(a) 128^3 systems (b) 256^3 systems

Figure 4.6: The magnetic energy spectra with each forcing method and similar Re plotted with each other. Diagram (a) shows systems of $Re \sim 105$ and (b) shows systems of $Re \sim 345$. Each diagram is plotted with the IK power law.

The diagrams each correspond to a different system size and contain the spectra from all forcing methods. The smaller system size runs appear to be largely in agreement with one another, and align with the IK spectrum at wavenumbers around: $2 < k < 10$, i.e. the inertial range after the wavenumber forced to in the simulation (the transfer spectra will clarify this). However, the 256^3 simulations agree with the IK spectrum to a much higher degree - as more wavenumbers are accessed in the larger system sizes. Recall that the IK and Kolmogorov spectra are assumed in the large Reynolds number limit, so it would be appropriate to assume from what we see in fig. 4.6 at larger system sizes/Re we would see a clearer power law in the spectra to a greater degree of accuracy. In the next subsection the time-averaged transfer functions from the energy spectra given here are presented.

Transfer Spectra

The transfer spectra tell us the net amount of energy transferred into any wavenumber. Figure 4.7 gives the magnetic and kinetic energy transfer spectra for all forcing methods at different system sizes. Referencing figure 4.6 (b) and (d), we see that our forcing is evident, given the negative values in the kinetic transfer spectra up to $k = 2$.

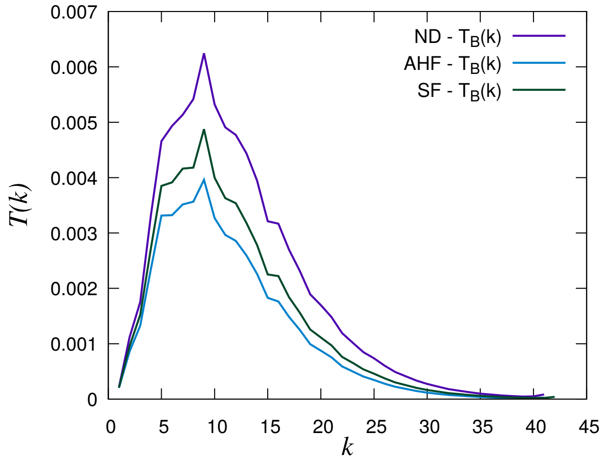

(a) 128^3 magnetic energy transfer

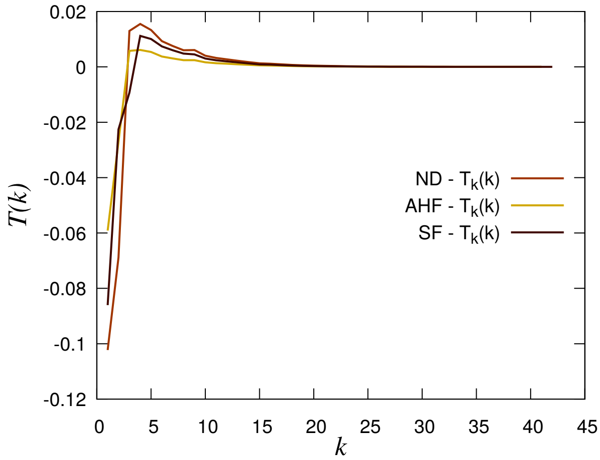

(b) 128^3 kinetic energy transfer

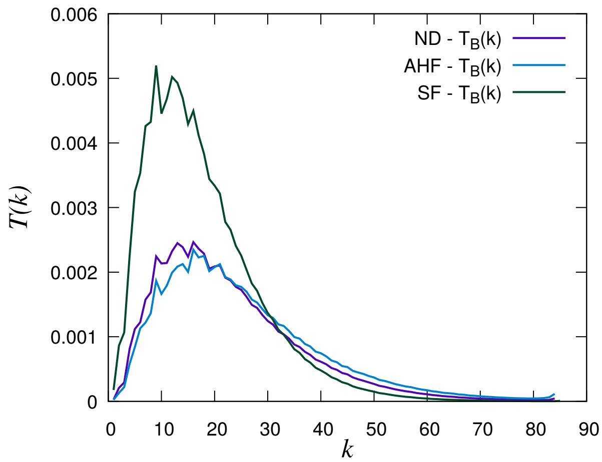

(c) 256^3 magnetic energy transfer

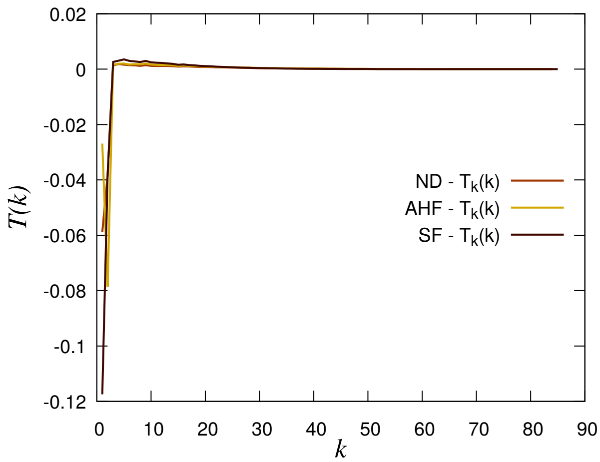

(d) 256^3 kinetic energy transfer

Figure 4.7: The ensemble average kinetic and magnetic transfer spectra for 128^3 and 256^3 and kinetic negative damping, adjustable helicity, and sinusoidal forcing. Negative values indicate energy flowing out of those wavenumbers, positive indicating energy is flowing in.

Transfer spectra doesn't necessarily depict the *action* of energy flowing between wavenumbers, but moreover gives an idea for where energy is stored (i.e. positive implies more energy is flowing into a specific wavenumber than out). In figure 4.7 we can see that kinetic energy is flowing out of the small forced wavenumbers and largely into the inertial range. As we have no forcing on our magnetic field, there is more energy entering into all wavenumbers in the magnetic transfer spectra than out. We can see that negative damping forcing dominates in spectra (a) and (b) and sinforcing dominates in (c) and (d). This is likely a cause of input parameters, as SF requires a higher forcing rate at larger system sizes and negative damping had a higher forcing rate than the other two for the 128^3 runs. Nevertheless, this is what we would expect from a kinetically forced simulation.

4.1.5 Kinetic Forcing Summary

This concludes our section on kinetic forcing, comparing results between each forcing type. We saw that each forcing method brings the systems to similar energetically steady states for multiple Reynolds number values. There were also some interesting magnetic/kinetic energy characteristics that developed. These were compared against the relative helicities, and with further analysis and computation a relevant relationship might emerge from these characteristic fluctuations between energy and helicity.

We also showed the different magnetic energy spectra between all forcing types, and saw the larger systems agreed with the IK spectrum to a certain extent. The IK spectrum is still up to debate, as it is similar in value to the Kolmogorov $-\frac{5}{3}$ power law. This could further be made clear with simulations of larger systems (e.g. 512^3 or 1024^3), as they encompass larger wave numbers (hence resolving at smaller scales). Along with the energy spectra, we examined the transfer spectra. We saw that indeed with kinetically forcing energy flows from large wavenumbers into the inertial range of magnetic and kinetic energy; shown by the negative values found in the kinetic transfer spectrum and uniformly positive values found in the magnetic transfer spectrum.

From the results presented in this section, we believe that there is an agreement with each kinetic forcing method through the observation of the similar energy spectra and the ideal conserved quantities. This shows what was expected, where the manner in which a system is forced doesn't matter at later times in MHD turbulence. This could better be clarified and confirmed through larger systems and longer simulation run times.

4.2 Magnetic and Kinetic Forcing

In this section we present our investigation of adding a magnetic forcing aspect to MHD turbulence through the AHF and ND forcing methods. In each simulation our kinetic and magnetic forcing rates were identical, $\mathrm{Pr} = 1$, and due to project time restrictions we only simulated system sizes of 128^3. All forcing referenced in this section will be both magnetic and kinetic, and the sole kinetic forcing studied in the prior section if mentioned will be explicitly stated as such. It was shown recently that magnetic sinusoidal forcing has the tendency to produce self-organized states when random phases were lessened [15]. A magnetic forcing could be visualized as something like an external magnetic field, whereas we only investigate in this report isotropic and homogeneous magnetic forcing.

Self-organized flows with ND in HD has been shown beforehand at low Reynolds numbers ($Re \sim 15 - 20$) [24], we wish to extend this to MHD at higher Reynolds numbers. This section is structured as follows. We begin with showing the energy, relative helicities, and energy spectra for ND magnetic/kinetic forcing. This brings about interesting results, where we see several large scale magnetic structures develop when observing the magnetic field iso-surface and flow diagrams. Then, we look at AHF magnetic/kinetic forcing and show the aforementioned values. Our investigation of AHF, however, shows results that are dissimilar to the ND method.

With longer simulation times and higher resolutions it could be clarified as to whether or not magnetic forcing should be treated to the same universal respect shown in the previous section with kinetic forcing. This section will largely be based on light speculation and presentation of findings. Due to the complicated nature of duly forcing a system, there is much at work in each simulation that could be up to many different interpretations.

4.2.1 Negative Damping Forcing

Figure 4.8 gives the energy over time for our negative damping forcing of both the magnetic and velocity fields. When first running the simulation for 100s of simulation time, we noticed a slightly horizontally asymptotic behaviour in both energies. We then extended the simulation time to 270s, and found that indeed it was asymptotically approaching some ceiling energy value (see fig. 4.8, $E_{tot} \sim 4.5s$). The energy curve for magnetic/kinetic ND presented in figure 4.8, at later times, agrees with what has been seen when MHD self-organizes through sinusoidal forcing [15].

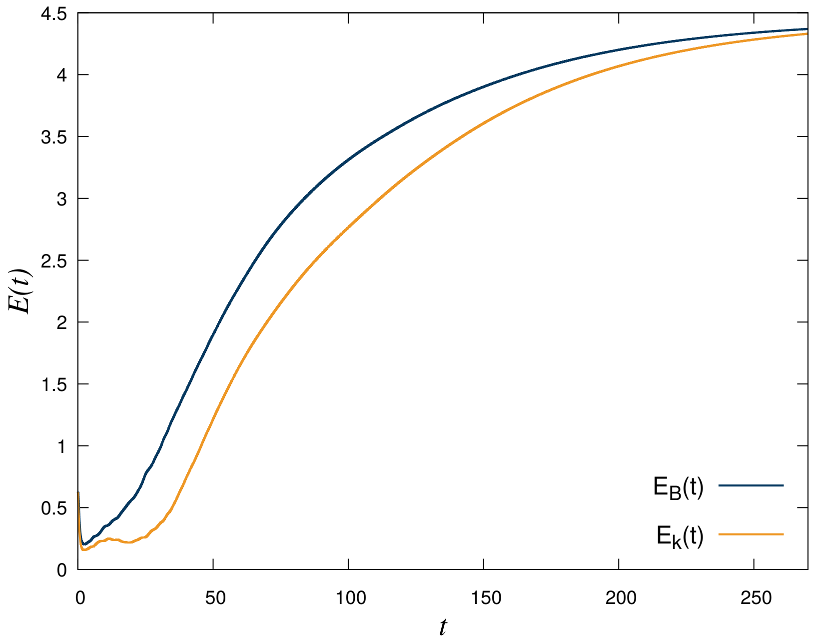

Figure 4.8: Energy for a 128^3 system forced with ND run for 270 seconds. Notice after 25 seconds there occurs a self-organized state.

The energy depicted in figure 4.8 above shows an end-state which is force-free ($\boldsymbol{j} \times \boldsymbol{B} = 0$) and Alfvénic ($\boldsymbol{U} \sim \pm\boldsymbol{B}$). Now, since $\boldsymbol{B}$ aligns with the current, $\boldsymbol{j} = \nabla \times \boldsymbol{B}$, then the Alfvénic nature of the system forces the velocity $\boldsymbol{U}$ to be Beltrami (since $\boldsymbol{U} \parallel \boldsymbol{B}$).

This then implies both fields are Beltrami, and the system is without non-linearity, hence there are no fluctuations seen after $\sim 25s$.

The relative helicities for the system depicted in figure 4.8 are given in figure 4.9 (a) and a different ND simulation that self-organized in (b).

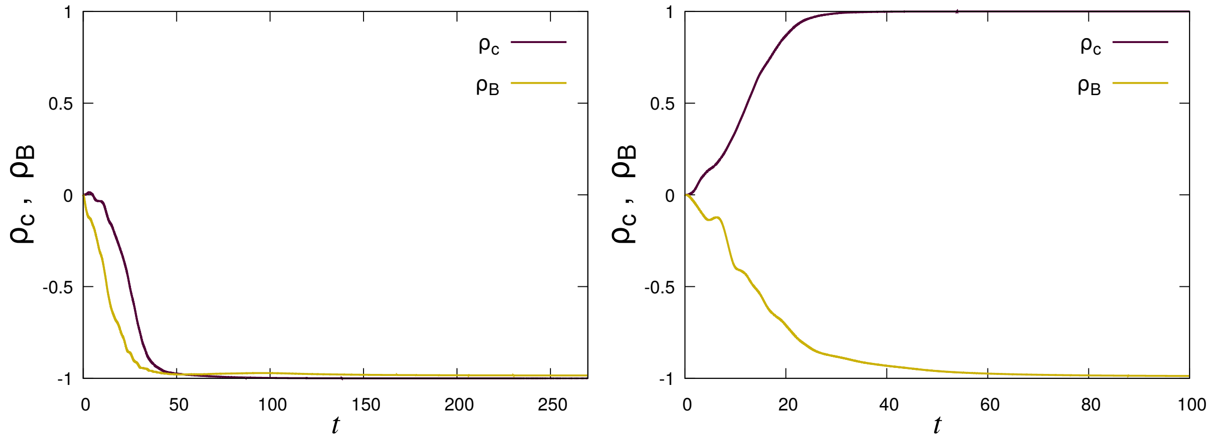

(a) ND, 128^3 Run Ac

(b) ND at 128^3, run A

Figure 4.9: Relative cross and magnetic helicities using ND forcing both kinetically and magnetically. Notice that though the simulations were nearly similar in their input parameters, they produce opposite valued cross helicities. This is due to the randomized initial directions of the $\boldsymbol{U}$ and $\boldsymbol{B}$ fields, in (b) we see they align together whereas (a) in they anti-align.

We can see that there is a strong dependence upon the initial conditions, depicted by the behaviours of the relative helicites in figure 4.9. Since the systems are almost immediately self-organizing, there are no inherent value fluctuations and the fields are given an anti-alignment/alignment immediately. Since the systems start without any initial helicity, the alignment is random (i.e. $\boldsymbol{U} \sim \pm\boldsymbol{B}$ and $\boldsymbol{B} \sim \pm\boldsymbol{j}$). This could be confirmed with a larger amount of statistics. It is also likely that due to the nature of ND and the manner of how it feeds the fields back into themselves, with zero initial helicity, once the direction of a field is assumed it will not alter.

We show the Alfvénic flow visualizations between the magnetic and kinetic fields in figure 4.10 at different time steps. Initially the system seems very chaotic (around $t = 20s$), however, it is seen that towards $t = 120s$, the fields become anti-aligned, agreeing with the relative helicity values shown in figure 4.9 (a).

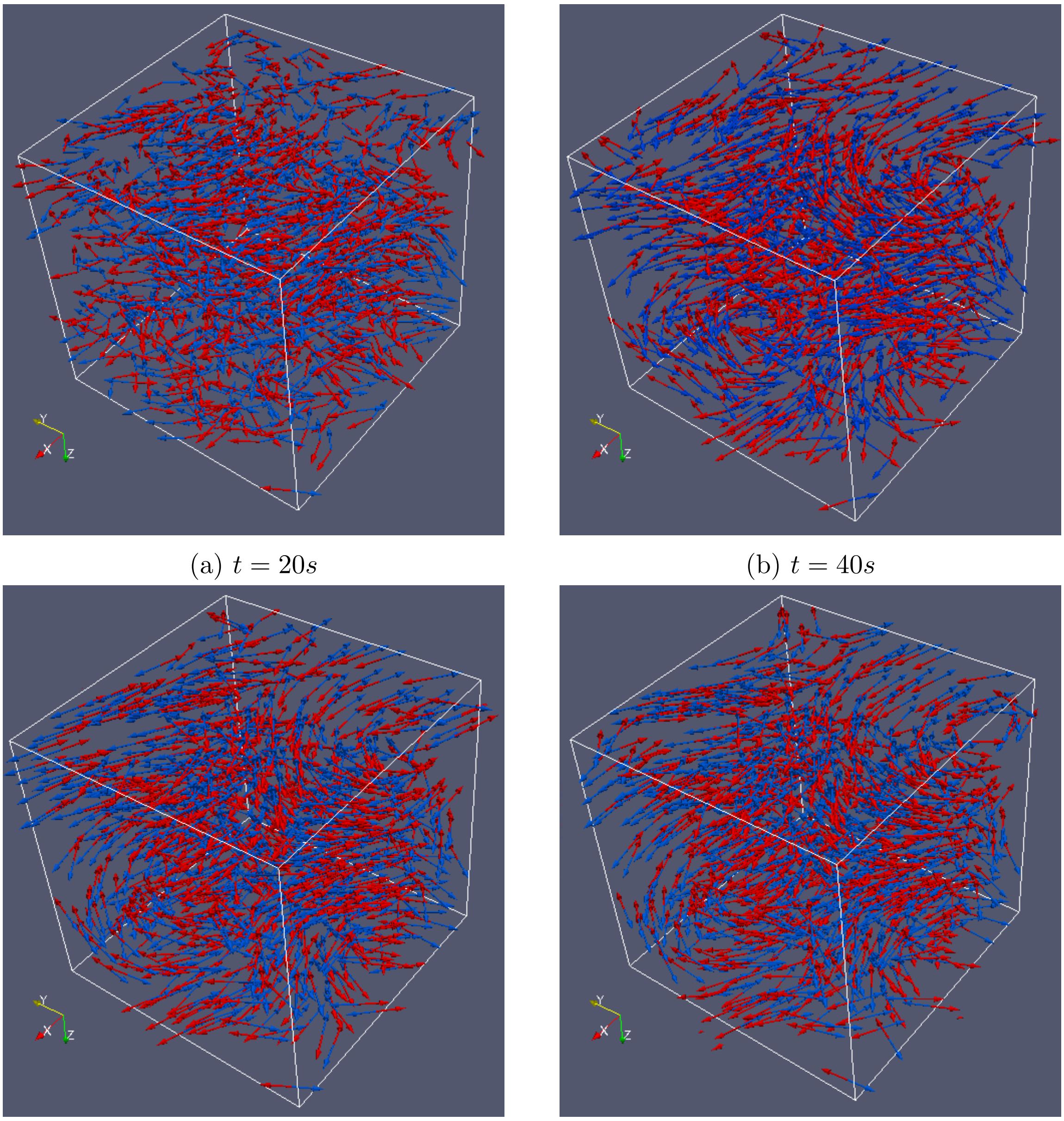

(a) $t = 20s$ (b) $t = 40s$

(c) $t = 60s$ (d) $t = 120s$

Figure 4.10: Flow visualizations of 128^3 ND kinetic and magnetic forcing at different simulation times. The blue vectors indicate the magnetic field, the red indicate the velocity field. Notice that as our simulation time increases, the fields become more Alfvénic and anti-aligned with each other ($\boldsymbol{U} \sim -\boldsymbol{B}$).

As figure 4.10 depicts, we see an increasing anti-alignment between the $\boldsymbol{U}$ and $\boldsymbol{B}$ fields. The white lines in the box depict our sample simulation volume. We can also aid in the visualization of the magnetic structures forming in these self-organized states through the depiction of iso-surfaces, shown in figure 4.11. These are colored by magnitude of the respective fields, the structures having the largest values near the red spectrum.

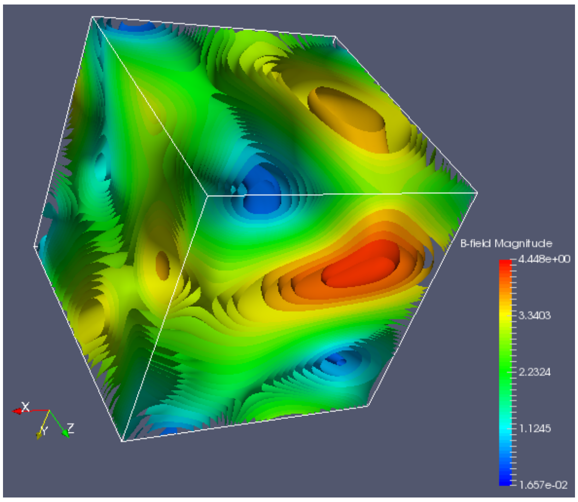

(a) Magnetic Field at $t = 100s$

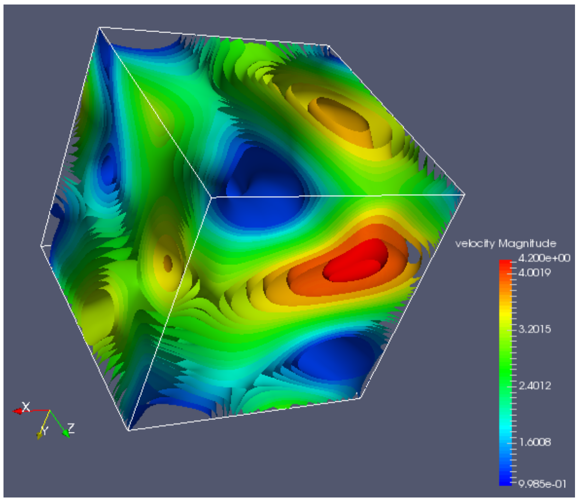

(b) Velocity field at $t = 100s$

Figure 4.11: Isosurfaces for the magntiude of the magnetic and velocity fields with ND magnetic/kinetic forcing at $t = 100s$. These depict large scale self-organized structures found in our flow.

We can see from figure 4.11 the presence of large scale magnetic structures in the system. At longer system times (e.g. $t = 1000s$) we predict a much larger amount of laminarization to occur. The behaviour we see in magnetic and kinetic ND is not seen when using similar inputs with AHF, however, which is shown in the next section.

4.2.2 Adjustable Helicity Forcing

In this section we present several simulations done kinetic and magnetic AHF forcing. This has brought interesting results that have deviated from the behaviours given in section 4.2.1 and described in Dallas et al. [15] report. It is possible that at longer run times similar behaviour might be found, but for the extent of the results in this section we only address simulation times of $100s - 130s$.

We structure this section differently than before, comparing three simulations with identical input values and differing seed values. The first two subsections show visualizations of our magnetic fields, and when comparing against the helicities it is apparent that the systems partially self-organize. Our first simulation shows an interesting increase in magnetic energy, followed by a $\sim 15s$ delay increase in kinetic energy. We sought to extend the run time for this simulation, but was met with a divergent time-step issue and decided to investigate through randomized seed values instead. This led to a second run being made, and we discovered a similar energetic form where a dramatic increase in magnetic energy occurred. When repeating the simulation and extending the time by

30s, we arrived at a curve and kinetic energy behaviour unlike our first. The third run depicts a possible unstable steady state, where we believe probabilistically the run has the ability to dramatically change magnetically at any point and likely diverge (as seen by the prior two run's results) or decrease back down.

Energy and Helicity Behaviours

We begin by observing the energy behaviours seen in figure 4.12. (a) shows the energy over time, where initially in the first $t = 10s - 45s$ a steady state appears, followed by a dramatic increase in magnetic energy. The relative helicities of the system are depicted in fig. 4.12 (b).

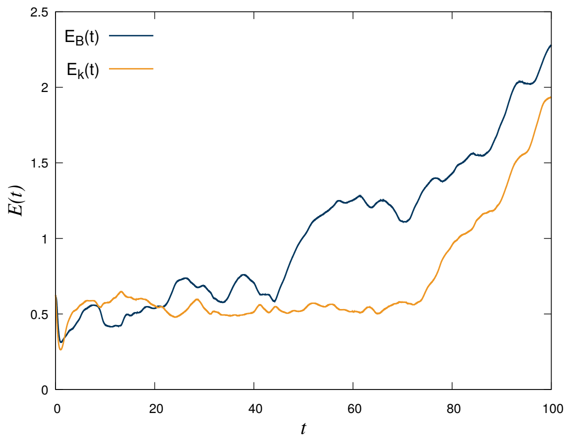

(a) Energy vs. time

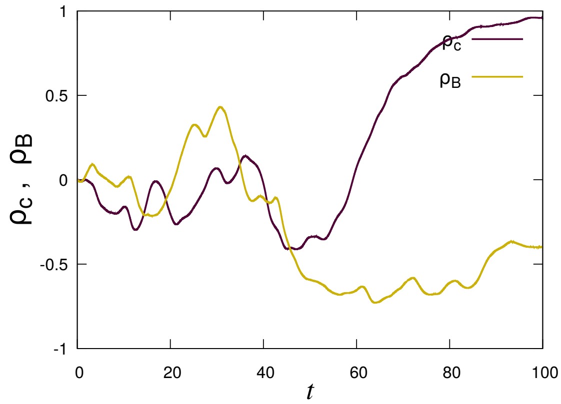

(b) Relative helicities

Figure 4.12: Run Bb, energy and relative helicities derived from AHF magnetic/kinetic forcing done on a system of size 128^3. Notice the interesting increase in magnetic energy in correlation to the relative cross helicity at $t \sim 50s$.

It appears that at $t \sim 50s$ a large spike of magnetic energy occurs, followed by a large value of cross helicity around 10s later. The relative CH is nonfluctuating at this point, and at $t = 80s$ the kinetic energy begins to increase rapidly as well. This results are up to speculation, but we believe that the strong alignment with both the velocity and magnetic fields causes a sort of 'cascading' buildup of energy, and the relative cross helicity exhibits a similar behaviour shown in the initial times of fig. 4.9 for kinetic/magnetic negative damping.

In the next simulation (figure 4.13), we ran identical parameters with a different seed to a total time of 100s, and noticed a similar buildup in magnetic energy towards the end of the run-time. This led us to believe a possible similar behaviour was happening close to what happened in figure 4.12, and we extended the simulation run-time by 30s. The curve, however, showed a kinetic energy that failed to increment in large amounts after 100s, and the magnetic energy appears to be returning back to the steady state it initially was in.

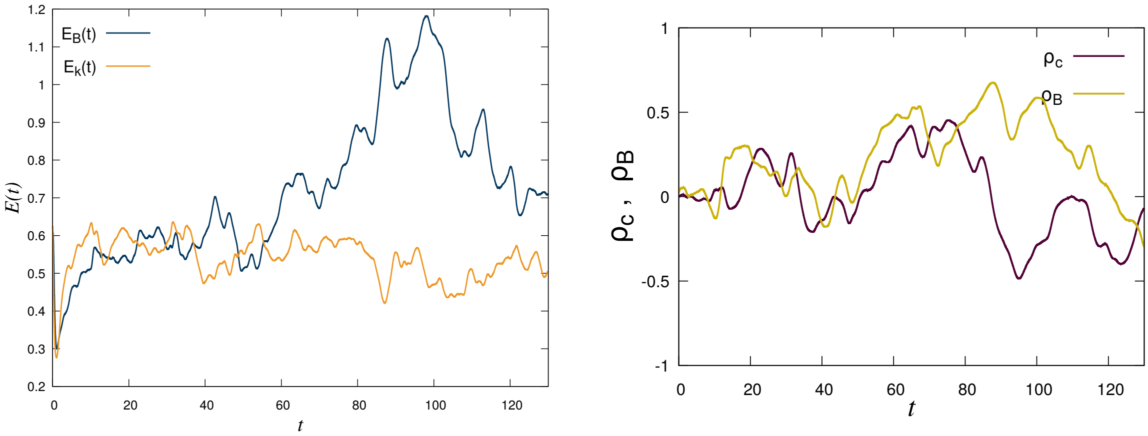

(a) Energy vs. time

(b) Relative helicities

Figure 4.13: Run Bb-s1, identical input parameters were used for this AHF magnetic/kinetically forced system of size 128^3, but a different seed value was introduced. The system exhibits a similar behaviour to what has been shown previously, but fails to emulate the actions of kinetic energy, magnetic energy, and relative CH.

Notice the relative helicity behaviours in figure 4.13 (b) exhibit very similar patterns to our first simulation in fig. 4.12 (b); although this time a sharp 'kink' occurs near $t = 90s$ and at the same time the magnetic energy sharply falls. This could be interpreted as a change in the alignments of the magnetic field due to AHF's ability to control relative helicity injection, and the system fails to accumulate energy as it did in fig. 4.12. It is also possible the alignments between the $\boldsymbol{U}$ and $\boldsymbol{B}$ fields are different in this simulation than in the first.

Finally, we present a third simulation in figure 4.14 with another random seed that shows a behaviour unlike the first two; namely, it simply resides within a quickly ascertained steady state (around $t = 10s$). The relative helicities depicted in fig. 4.14 (b) give an initial behaviour similar to our previous two runs, but show no large amounts of relative CH buildup.

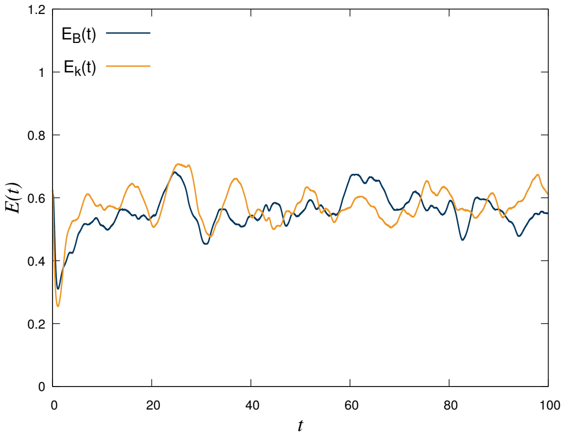

(a) Energy vs. time

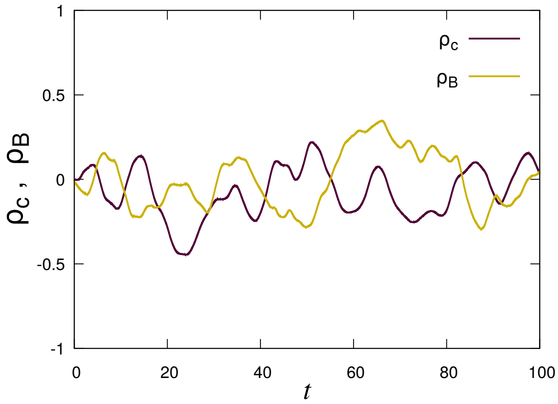

(b) Relative helicities

Figure 4.14: Run Bb-s2, a third run of identical parameters with a different seed for AHF kinetic/magnetic forcing on system sizes of 128^3. We note that the behaviours seen in this system differ from both, given there are no large scale fluctuations in energy or relative helicity.

This behaviour then leads us to believe that magnetically and kinetically forcing an MHD with randomly seeded AHF could lead to the possibility of three different states depicted in figures 4.12 - 4.14. The nature of what is happening could largely be dependent upon the behaviour of the helicity (i.e. the alignment of the fields) and possibly how AHF alters it. Again, this is still up to a fair amount of speculation, and a statistical approach with many different seeded runs should be taken to help further characterize what happens with this particular method of AHF forcing.

Following our initial speculation for kinetic forcing, where the end state should be independent of the manner in which a system was forced, we question whether this could apply to kinetic/magnetic forcing. We have shown that the self-organization occurring with SF (through [15]) and ND is similar, but with AHF differently acting systems are produced at long run-times ($100s - 120s$). As ND shows an almost immediate alignment of fields, it is up to question whether or not there is any self-organization seen within the AHF systems. Our speculation is that there is with certain systems, slightly, given the large fluctuations in helicity values and the energy build-ups seen in figure 4.12. This can be seen through the visualizations of the magnetic fields, given in figure 4.15. These depict partially developing magnetic structures.

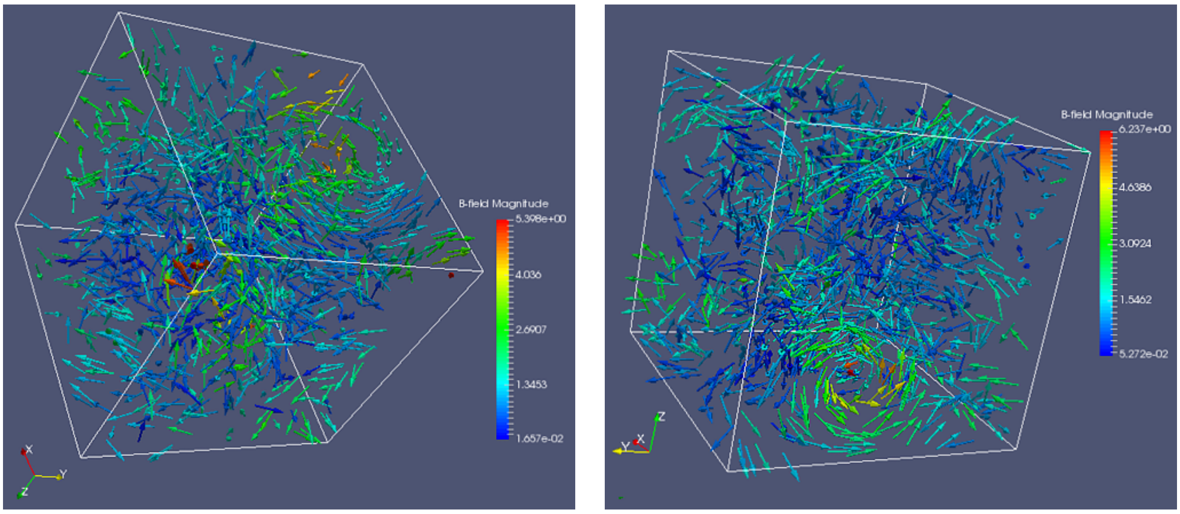

(a) Run Bb, $t = 60s$ (b) Run Bb-s1, $t = 100s$

Figure 4.15: Flow visualizations for the magnetic fields from the first two presented runs, colors depict the magnitude of the field's vectors (red being the highest). Several partially self-organized structures can be seen, depicted by the spirals shown in the field lines.

The figures shown in figure 4.15 depict the magnetic fields and partially self-organized structures within them. These are both at times where the magnetic field in the systems have spiked and locally maximized. It is possible that the partial alignments are what is causing the harsh fluctuations in the relative cross helicities - giving a probability that the cross helicity maximizes and a buildup of energy occurs like what was seen with ND. This could be further confirmed or disregarded with more statistics.

4.2.3 Magnetic Forcing Summary

This concludes our section of magnetic/kinetic forcing with ND and AHF. We have seen the interesting behaviours of negative damping, where an almost immediate self-organization occurs. We also saw that as run-times are extended, the energies approach a horizontally asymptotic value. We found that the both fields were Alfvénic and Beltrami, given that $\boldsymbol{B}$ was initially Beltrami and $\boldsymbol{U} \parallel \boldsymbol{B}$ over time, this was visualized in figures 4.10 and in 4.11. Where the latter showed iso-surfaces of the magnetic and velocity field magnitudes.

The second portion of this section showed AHF magnetic/kinetic forcing, giving different results in comparison to to ND. From the visualizations of the magnetic fields presented in figure 4.15, we saw partially developed self-organized states. The different seed values also gave randomized behaviours in the energy and relative helicities, where each run either showed a buildup of both energies/maximizing of CH, a sudden buildup of magnetic energy with CH - but returning back to steady state, or a steady state run exhibiting none of the characteristics the first two showed. This calls into question the assumption we made with kinetic forcing, where the non-linearity of turbulence disregards a reliance on initial forcing methods, and could possibly not pertain to magnetic/kinetically forced MHD. We leave it for further investigation to accurately characterize these flows.

Chapter 5

Conclusions

In this report, we investigated the characteristics of energetically steady state 3-D Magnetohydrodynamic statistically homogeneous and isotropic turbulent flows. These were simulated through three different forcing methods, used to agitate the system into a turbulent state after a short simulation time period.

We first began by investigating systems that were solely kinetically forced. Our results, as expected, showed similar behaviours between each forcing method. The energy over time plots depicted when the systems moved into a steady state (energy dissipating is equal to energy being introduced) and confirmed the presence of the dynamo effect. The magnetic spectra gave us confirmation that the systems behaved similarly, where a possible alignment with the IK spectra was noted and each forcing method produced nearly identical curves. The magnetic and kinetic transfer spectra also agreed with each method of kinetic forcing, and we found these to be in agreement with what was theoretically expected as energy was leaving lower wavenumbers in our kinetic spectrum and entering through every wavenumber in the magnetic spectrum.

We also saw interesting results with magnetic/kinetic forcing using both negative damping and adjustable helicity. It was seen that the negative damping almost immediately self-organized, and as simulation time continued the flows ran asymptotically towards a further state of laminarization. This was made evident by the relative helicity behaviours (fig. 4.9) and energy over time plot, indicating an Alfvénic state between the $\boldsymbol{U}$ and $\boldsymbol{B}$ fields. We confirmed this through the 3-D visualization of the magnetic and velocity field vectors, where the fields were perfectly anti-aligned with one another at later system times. Similar results of self-organization have been seen before through specific randomized SF in MHD [15].

Magnetic and kinetic forcing with AHF, however, only partially self-organized, as we saw in the large scale magnetic structures shown in figure 4.15. With several differently seeded runs, we noticed varying behaviours within the energy and relative helicity plots. We believe the peculiar behaviour could be partially due to the fact that there is a randomizing factor in AHF, as discussed in section 3.3.2, where each forcing step creates two vectors that are eigenfunctions of the curl operator and non-parallel to a random $\boldsymbol{k}$ [37]. These results are still up for much speculation, and were of relatively low sample sizes (128^3). What was interesting was the behaviour given in figure 4.12 where the relative cross helicity and the magnetic energy seemed to increase away from its normal steady state fluctuations. This in turn caused the kinetic energy to suddenly increase, either from the Lorentz term in the N-S MHD eqn. 2.45 or the buildup of cross helicity.

In all cases, there is still much work to be achieved through the results presented here. Simulations with larger amounts of randomly seeded iterations and larger Reynolds numbers would be needed to further confirm what we have presented.

Future Work

To continue our results, it is recommended that larger system sizes (up to 1024^3) be run for each forcing method and over several different iterations. A statistically averaged magnetic energy spectra at these Reynolds numbers could help clarify the large Re limit and see whether it agrees with the IK spectrum, the Kolmogorov spectrum, or something else entirely.

The same argument should be made for the magnetic/kinetic forcing. It would be viable to create several simulations that force magnetically and not kinetically. This would help characterize how magnetic forcing independently affects the system's outputs. For the investigation of negative damping with magnetic/kinetic, larger system sizes and longer run times (e.g. $t = 1000s$) should be done in order to investigate any interesting behaviours once when the fields are fully aligned. Magnetic/kinetic AHF should be approached in a much more statistical fashion, where iterative runs at small Reynolds numbers are simulated for larger amounts of time ($t = 200s - 300s$).

Appendix A

Run Input Parameters

A.1 Input Parameters

In this short appendix we give a partial list of simulation parameters for simulations that mostly completed (run times were at or exceeded $t \sim 70s$). Forcing methods are described in the captions and under the **Forcing Type** category.

Forcing Type	**Run ID**	**System Size**	$\boldsymbol{\nu}$	**Forcing Rate**	**dt**	**Run Time**
Negative Damping	A	128^3	0.01	0.1	0.001	$100sec.$
	C	128^3	0.015	0.1	0.001	$100sec.$
	D	128^3	0.02	0.1	0.001	$100sec.$
	E	128^3	0.0023	0.2	0.001	$100sec.$
	C1	256^3	0.0023	0.1	0.001	$100sec.$
	D1	256^3	0.0023	0.1	0.001	$69.78sec.$
	Db1	256^3	0.0018	0.2	0.001	$70.43sec.$
AHF	A	128^3	0.01	0.1	0.001	$100sec.$
	C1	128^3	0.008	0.1	0.001	$100sec.$
	D1	128^3	0.013	0.1	0.001	$100sec.$
	Fa	256^3	0.0023	0.01	0.001	$100sec.$
	Fb	256^3	0.0018	0.01	0.001	$100sec.$
	H1	256^3	0.0023	0.012	0.001	$100sec.$
SF	Da	128^3	0.01	0.3	0.01	$100sec.$
	E1	128^3	0.008	0.3	0.001	$100sec.$
	F1	128^3	0.01	0.4	0.001	$100sec.$
	G1	128^3	0.012	0.3	0.001	$100sec.$
	H1	128^3	0.012	0.3	0.001	$100sec.$
	D1	256^3	0.0014	0.3	0.001	$100sec.$
	J	256^3	0.0032	0.36	0.001	$100sec.$
	K	256^3	0.004	0.36	0.001	$100sec.$

Table A.1: A list of basic run parameters used for kinetically forcing MHD systems. Systems with run times $< 100s$ were not included in our results.

Forcing Type	**Run ID**	**System Size**	$\boldsymbol{\nu}$	**Forcing Rate**	**dt**	**Run Time**
Negative Damping	A	128^3	0.009	0.1	0.001	$100sec.$
	Aa	128^3	0.009	0.08	0.001	$200sec.$
	Ac	128^3	0.009	0.08	0.001	$270sec.$
	Ad	128^3	0.009	0.08	0.001	$170sec.$
AHF	B	128^3	0.01	0.1	0.001	$100sec.$
	Bb	128^3	0.01	0.02	0.001	$100sec.$
	Bb-s1	128^3	0.01	0.02	0.001	$100sec.$
	Bb-s3	128^3	0.01	0.02	0.001	$100sec.$
	Bb-s5	128^3	0.01	0.02	0.001	$100sec.$
	xt-s1	128^3	0.01	0.02	0.001	$130sec.$

Table A.2: A list of basic run parameters used for magnetic/kinetic forcing in MHD systems. Systems with run times $< 100s$ were not included in our results.

Bibliography

[1] P. A. Davidson. *An Introduction to Magnetohydrodynamics*. Cambridge University Press, 2001.

[2] A. N. Kolmogorov. Dissipation of energy in the locally isotropic turbulence. *Proceedings of the Royal Society of London A: Mathematical, Physical and Engineering Sciences*, 434(1890):15–17, 1991.

[3] S. R. Yoffe. *Investigation of the transfer and dissipation of energy in isotropic turbulence*. Ph.D. Thesis. University of Edinburgh, 2012.

[4] M. F. Linkmann. *Self-organisation processes in (magneto)hydrodynamic turbulence*. PhD thesis, University of Edinburgh, 2016.

[5] James M. Stone and James E. Pringle. Magnetohydrodynamical non-radiative accretion flows in two dimensions. *Monthly Notices of the Royal Astronomical Society*, 322(3):461–472, 2001.

[6] John F. Hawley, Steven A. Balbus, and James M. Stone. A magnetohydrodynamic nonradiative accretion flow in three dimensions. *The Astrophysical Journal Letters*, 554(1):L49, 2001.

[7] Moreau Rene J., S. Molokov, and H. K. Moffatt. *Magnetohydrodynamics: historical evolution and trends*. Springer, 2007.

[8] E. E. Goldstraw. *Large Scale Forcing In Magnetohydrodynamic Turbulence*. Ph.D. Thesis. University of Edinburgh, 2015.

[9] D. Clark. A comparison of forcing functions in magnetohydrodynamic turbulence. Master's thesis, University of Edinburgh, 2016.

[10] Osborne Reynolds. An experimental investigation of the circumstances which determine whether the motion of water shall be direct or sinuous, and of the law of resistance in parallel channels. *Philosophical Transactions of the Royal Society of London*, 174:935–982, 1883.

[11] A. N. Kolmogorov. The local structure of turbulence in incompressible viscous fluid for very large reynolds numbers. *Proceedings of the Royal Society of London A: Mathematical, Physical and Engineering Sciences*, 434(1890):9–13, 1991.

[12] S. B. Pope. *Turbulent Flows*. Cambridge University Press, 2000.

[13] U. Frisch and A. N. Kolmogorov. *Turbulence: the Legacy of A.N. Kolmogorov.* Cambridge University Press, 1995.

[14] W. D. McComb. *The Physics of Fluid Turbulence.* Oxford University Press, 1992.

[15] V. Dallas and A. Alexakis. Self-organisation and non-linear dynamics in driven magnetohydrodynamic turbulent flows. *Physics of Fluids*, 27(4), 2015.

[16] D. Biskamp. *Magnetohydrodynamic Turbulence.* Cambridge University Press, 2003.

[17] Arjun Berera and Moritz Linkmann. Magnetic helicity and the evolution of decaying magnetohydrodynamic turbulence. *Phys. Rev. E*, 90:041003, Oct 2014.

[18] P.S. Iroshnikov. Turbulence of a conducting fluid in a strong magnetic field. *sovast*, 7:566, feb 1964.

[19] R. H. Kraichnan. Inertialrange spectrum of hydromagnetic turbulence. *Physics of Fluids*, 8(7), 1965.

[20] S. Oughton and R. Prandi. Kinetic helicity and mhd turbulence. *Journal of Plasma Physics*, 64:179–193, 8 2000.

[21] Dalton D. Schnack. *Lectures in Magnetohydrodynamics: with an appendix on extended MHD.* Springer, 2009.

[22] K.-H. Rädler. *Mean-Field Magnetohydrodynamics as a Basis of Solar Dynamo Theory*, pages 323–344. Springer Netherlands, Dordrecht, 1976.

[23] M. F. Linkmann, A. Berera, W. D. McComb, and M. E. McKay. Nonuniversality and finite dissipation in decaying magnetohydrodynamic turbulence. *Phys. Rev. Lett.*, 114:235001, Jun 2015.

[24] W. D. McComb and S. R. Yoffe B. Jankauskas M. F. Linkmann, A. Berera. Self-organization and transition to turbulence in isotropic fluid motion driven by negative damping at low wavenumbers. *Journal of Physics A: Mathematical and Theoretical*, 48(25):25FT01, 2015.

[25] M Aschwanden. Self-organized criticality phenomena. *Self-Organized Criticality in Astrophysics*, page 135, 2010.

[26] Ryusuke Numata, Zensho Yoshida, and Takaya Hayashi. Nonlinear three-dimensional simulation for self-organization and flow generation in two-fluid plasmas. *Computer Physics Communications*, 164(1-3):291296, 2004.

[27] M. Roberts, M. Leroy, J. Morales, W. Bos, and K. Schneider. Self-organization of helically forced mhd flow in confined cylindrical geometries. *Fluid Dynamics Research*, 46(6):061422, 2014.

[28] Dalton D. Schnack. *Lectures in magnetohydrodynamics: with an appendix on extended MHD, Ch. 17, 37.* Springer, 2009.

[29] M. Dobrowolny, A. Mangeney, and P. Veltri. Fully developed anisotropic hydromagnetic turbulence in interplanetary space. *Phys. Rev. Lett. Physical Review Letters*, 45(2):144147, 1980.

[30] U. Frisch, A. Pouquet, J. LOrat, and A. Mazure. Possibility of an inverse cascade of magnetic helicity in magnetohydrodynamic turbulence. *Journal of Fluid Mechanics*, 68:769–778, 4 1975.

[31] A. Alexakis, P. D. Mininni, and A. Pouquet. On the inverse cascade of magnetic helicity. *The Astrophysical Journal*, 640(1):335, 2006.

[32] P. D. Mininni, A. Alexakis, and A. Pouquet. Scale interactions and scaling laws in rotating flows at moderate rossby numbers and large reynolds numbers. *Physics of Fluids*, 21(1), 2009.

[33] G A Glatzmaier, R S Coe, L H Hongre, and P H Roberts. The role of the earth's mantle in controlling the frequency of geomagnetic reversals. *Nature*, 401:885890, Oct 1999.

[34] J. Smagorinsky. General circulation experiments with the primitive equations. *Mon. Wea. Rev. Monthly Weather Review*, 91(3):104105, 1963.

[35] Charles Hirsch. *Numerical Computation of Internal and External Flows, Vol 1: Fundamentals of Computational Fluid Dynamics*, volume 1. Elsevier/Butterworth-Heinemann, 2 edition, 2007.

[36] L. Machiels. Predictability of small-scale motion in isotropic fluid turbulence. *Phys. Rev. Lett.*, 79:3411–3414, Nov 1997.

[37] A. Brandenburg. The inverse cascade and nonlinear alphaeffect in simulations of isotropic helical hydromagnetic turbulence. *ApJ, The Astrophysical Journal*, 550(2):824840, 2001.